Apparatus for Measuring Air Gap and Rotor Position in Linear Motors

Master's Thesis,

Henry Piitulainen

School of Electrical Engineering

Thesis Supervisor:

Prof. Marko Hinkkanen

Thesis advisor:

M.Sc. Antti Kallioniemi

Author: Henry Piitulainen

Title: Apparatus for Measuring Air Gap and Rotor Position in Linear Motors

Date: 9.6.2017 Language: English Number of pages: 83

Department of Electrical Engineering and Automation

Professorship: Electric Drives Code: S-81

Supervisor: Prof. Marko Hinkkanen

Advisor: M.Sc. Antti Kallioniemi

This thesis studies inductive air gap and rotor position sensing in linear motors. The object is to find a sensing apparatus for an industrial application. Therefore, inductive sensing is studied and requirements for the sensing apparatus are defined. Inductive position sensing is further developed to suit the application, a sensing apparatus is designed and a prototype is manufactured. Also, a test arrangement is designed and built and the prototype is tested. Test results verify that the designed sensing apparatus meets the requirements and a further development could be worthwhile.

Keywords: air gap sensing, rotor position, inductive sensor

AALTO-YLIOPISTO DIPLOMITYÖN

SÄHKÖTEKNIIKAN KORKEAKOULU TIIVISTELMÄ

Tekijä: Henry Piitulainen

Työn nimi: laite ilmavälin ja roottorin paikan mittaamiseen lineaarimoottoreissa

Päivämäärä: 9.6.2017 Kieli: englanti Sivumäärä: 83

Sähkötekniikan ja automaation laitos

Professuuri: sähkökäytöt Koodi: S-81

Valvoja: Prof. Marko Hinkkanen

Ohjaaja: DI Antti Kallioniemi

Tämä diplomityö tutkii induktiivista ilmavälin ja roottoripaikan mittausta lineaarimoottorikäytöissä. Työn tavoite on löytää toteuttamiskelpoinen mittalaite teolliseen sovelluskohteeseen. Sen vuoksi työssä tutkitaan induktiivista mittausta ja määritetään vaatimukset mittalaitteelle. Induktiivista paikanmittausta kehitetään edelleen sopimaan sovelluskohteeseen, mittalaite suunnitellaan ja siitä valmistetaan prototyyppi. Lisäksi suunnitellaan ja rakennetaan testausjärjestely, jolla prototyyppi testataan. Testitulokset todentavat, että mittalaite saavuttaa sille asetetut vaatimukset sekä sen, että mittalaitteen kehittämistä kannattaa jatkaa.

Avainsanat: ilmavälin mittaus, induktiivinen anturi, roottorin paikka

Preface

This thesis was done for a research project of KONE Corporation. KONE provided premises at Hyvinkää for writing and experimental part of the work. The experimental work utilized measuring instruments and equipment of R&D laboratory. This thesis was financed by KONE.

Several people participated my work and first, I would like to thank my supervisor professor Marko Hinkkanen and my instructor Antti Kallioniemi for their valuable guidance and support. Special thanks go to Tero Hakala, Tuukka Korhonen, Seppo Suur-Askola, Pasi Raassina and Tero Purosto for sharing their knowledge, guidance and flexible procurement of resources needed in this work. In addition, I would like to thank Ilpo Kauhaniemi and Marko Minkkinen for their help relating to the building of the test arrangement. Also, I would like to thank Marika Vainio for her help concerning proto PCBs and measurement arrangements.

This thesis required a lot of my leisure time and therefore, I would like to thank my family and close ones for their support and understanding.

Espoo, Finland

June 2017

Henry Piitulainen

Esipuhe

Tämä diplomityö tehtiin Kone Oyj:n tutkimushankkeeseen. Kone tarjosi tilat työn kirjoittamista sekä kokeellista osaa varten Hyvinkään toimipisteeltä. Kokeellisessa osassa hyödynnettiin tuotekehityslaboratorion mittalaitteita ja tarvikkeita. Työ on rahoitettu Koneen puolesta.

Moni osallistui työhöni ja ensimmäiseksi haluaisin kiittää valvojaani professori Marko Hinkkasta ja ohjaajaani Antti Kallioniemeä heidän tarjoamasta arvokkaasta ohjauksesta ja tuesta. Erityiset kiitokset ansaitsevat myös Tero Hakala, Tuukka Korhonen, Seppo Suur-Askola, Pasi Raassina ja Tero Purosto heidän jakamasta osaamisestaan, ohjauksesta ja joustavasta toiminnasta työssä tarvittujen resurssien hankintoihin liittyen. Lisäksi haluaisin kiittää Ilpo Kauhaniemeä ja Marko Minkkistä avusta testipenkin rakennuksessa sekä Marika Vainiota avusta protopiirikorttien valmistuksessa ja mittausjärjestelyissä.

Diplomityö vaati paljon vapaa-aikaani ja sen vuoksi haluaisin kiittää perhettäni ja läheisiäni heidän jatkuvasta tuesta ja ymmärryksestä.

Espoo, Suomi

Kesäkuu 2017

Henry Piitulainen

Contents

Symbols and abbreviations

Symbols and Units

A	[m^2]	Cross-sectional area of a magnetic flux
A_m	[m^2]	Cross-sectional area of a magnetic circuit
C_{RC}	[F]	Capacitance of resonance circuit
D		Difference signal
I	[A]	Current
L	[H], [Wb/A]	Inductance
L_{RC}	[H], [Wb/A]	Equivalent inductance of the resonance circuit
N		Number of turns in a coil
P_D		Phase table
$\mathcal{R}_m$	[1/H]	Reluctance
R_{RC}	[V/A], [Ω]	Resistance of the resonance circuit
S		Resonance circuit output signal
T_{sw}	[s]	Switching period
T		Look-up method threshold limit
V_{CC}	[V]	Buck converter input voltage
V_{DD}	[V]	Operating voltage
f_{CLKIN}	[1/s], [Hz]	Reference clock frequency
f_{RC}	[1/s], [Hz]	Resonance frequency of the resonance circuit
l	[m]	Length of a magnetic flux path
l_H	[m]	Height of a stator rail tooth
l_M	[m]	Distance between two measurements
l_m	[m]	Length of a magnetic circuit
l_{PP}	[m]	Pole pitch
l_S	[m]	Distance between stator rail teeth
l_T	[m]	Length of a stator rail tooth
l_W	[m]	Width of a stator rail
n_B		Number of communicated bytes
n_C		Settable A/D converter parameter

t	[s]	Time
t_c	[s]	Conversion time
t_M	[s]	Measurement time
t_{PCP}	[s]	Post-conversion processing time
t_{SPI}	[s]	Master-slave communication time
t_{R1}	[s]	First response time
t_{R2}	[s]	Second response time
$t_{switching}$	[s]	Switching time
v_m	[m/s]	Velocity of the mover
y		A/D converter output value
Φ	[Tm^2], [Wb]	Magnetic flux
μ	[H/m]	Permeability
μ_r	[H/m]	Relative permeability
μ_0	[H/m]	Vacuum permeability

Abbreviations

AC	Alternating current
A/D	Analog-to-digital
CSB	Chip select bus
DC	Direct current
EPCB	Electronics printed circuit board
Maglev	Magnetically levitated
MISO	Master input slave output line
MOSI	Master output slave input line
PCB	Printed circuit board
PMLM	Permanent magnet linear motor
PWM	Pulse-width modulation
SCLK	Serial clock line
SPCB	Sensor printed circuit board
SPI	Serial peripheral interface

1 Introduction

In this chapter, a linear motor concept will be briefly discussed and to motivate the reader, some challenges and benefits relating to linear motor applications will be presented. In addition, the research problem and objectives will be defined.

1.1 Background

Conventional rotating electric machines comprise a stationary cylindrical stator and a rotating rotor. Linear motors comprise a linear stator, which is also stationary, and a mover, i.e. rotor, which can move along the linear stator rail. Current linear motor technology enables to choose between a simplified stator topology with more complicated mover structure or a simplified mover topology with more complex stator. Basically, simplified mover topology means that there are windings in the stator side which are typically controlled with a frequency converter, and the mover includes for instance permanent magnets. On the other hand, simplified stator topology means that the stator is designed to conduct magnetic flux in a way that force and therefore motion can be provided with correctly controlled flux from the mover part. An example could be a stator with permanent magnets on the surface, a mover including multi-phase winding and a frequency converter which supplies alternating currents to the mover winding. The most suitable linear motor topology depends on the application itself, but linear motor technology enables various possibilities to redesign former applications for instance assembly line designs and means of transportation.

Compared to conventional rotating electric machines, linear motors are usually more expensive as the stator covers whole operation range and therefore requires more materials. However, linear motor solutions can simplify some applications because they do not require for instance transmissions, they have less wearing parts and, in case of magnetically levitating (Maglev) solutions, they lack friction. Especially, in high speed applications, for instance in Maglev trains, the frictionless magnetic levitation is utilized

to reach higher velocities. Nevertheless, magnetic levitation sets strict and unconditional requirements for an air gap between the mover and the stator rail. If for instance previously mentioned Maglev train makes contact with a stator rail at its top speed, approximately 500 km/h, the consequences can be devastating. The control of electric machines requires exact information about the angle of the rotor, or in the linear applications, information about the mover position relative to the stator rail. Otherwise, the performance is poor or in the worst case the machine cannot operate at all. Therefore, this information must be obtained somehow. Commonly, it is acquired by measuring it directly with encoders or other absolute position sensors. Another way is to estimate it with frequency converter variables e.g. with measured currents, voltages etc. Moreover, estimating requires more sophisticated control algorithms and even if such are developed, some applications require absolute position information by default because of valid regulations, standards, legislation etc.

Control of linear motors can be obtained with expensive sensing devices or estimates. However, mass production requires feasible rotor position sensing solution with minimized expenses. This thesis studies and provides a possible solution for linear motor air gap and rotor position sensing. By providing such an apparatus, linear motor applications could displace some current electric machine applications on the markets.

1.2 Research Problem and Objective

This thesis studies a permanent magnet linear motor (PMLM) application with a simplified stator topology. The mover comprises permanent magnets and multi-phase winding. Additionally, the mover is not attached to the stator rail by any means. Therefore, the application is entirely based on levitation. Control of the air gap is crucial for the operation so it must be executed accurately. The system is labile by its nature, which means that in case it encounters a disturbance and the mover is unbalanced the forces affecting to it will change exponentially. Without a fast response from the control system, the mover and the stator rail will make contact. Hence, the accuracy of the air gap sensing is essential, but from the control point of view, measurement time is more important. Furthermore, motion control requires accurate information about the mover

position in relation to the stator. However, this does not have such strict measurement time requirements.

The main objective for this thesis is to develop a sensing apparatus which provides fast and accurate air gap and position information for the control system of PMLM. The main objective is further divided into four sub-objectives. First one is to perform a background study of a potential sensing solution. Second sub-objective is to develop a sensing apparatus based on the studied sensing solution. Third sub-objective is to develop a test system for this sensing apparatus which will be suitable to test air gap and rotor position sensing. Last sub-objective is to test and evaluate the developed sensing apparatus with the developed test system.

2 Overview of Relevant Sensing Technology

First in this chapter basics in inductive sensing are discussed. Then a rotor position sensing solution of a similar commercial linear motor application is described. These topics are introduced because they form the basis for the design of the sensing apparatus.

2.1 Inductive Sensing

Inductive sensors measure ambient inductance of a sensing coil. Additionally, inductive proximity sensors convert this inductance to a proximity information. This conversion however requires that either the properties of ambient materials are known or the sensor is calibrated with an external reference.

Inductive sensors can measure the presence of materials which are either electrically or magnetically conductive. Generally, inductive sensors comprise a sensing coil which is supplied with a current. This generates a magnetic field around the sensing coil. Surrounding materials which are magnetically conductive affect to a measured inductance value because the flow of magnetic flux changes. As for electrically conductive materials, the change in magnetic field generates eddy currents according to Lenz's law. The direction of eddy currents is such that the change in the original magnetic field is resisted. This phenomenon can be sensed as an increased power consumption or change in impedance, current or voltage of the sensing coil.

Therefore, inductive sensors can sense the proximity of electrically conductive materials if the material is moving in such a way that eddy currents are induced to it or the sensing coil is supplied with and alternating current (AC) which generates alternating magnetic field around the sensing coil. The ability to sense these materials is reduced significantly if their structure is such that the flow of eddy currents is prevented. A laminated electrical steel is a good example of a material which decreases eddy currents depending on the angle between the magnetic field and the layers of laminated steel (Pippuri, 2010).

Some inductive proximity sensors supply AC to a sensing coil to generate alternating

magnetic field (Guaraglia & Pousa, 2014). However, resistive losses between the sensing coil and a power supply can be reduced, using a resonance circuit comprising a capacitor in parallel with the sensing coil as is used in a publication (Suhas & Oberhauser, 2016) concerning a motor speed and position sensing. Hence, energy transfers between the magnetic field of the sensing coil and the electrical field of the capacitor. This resonance circuit oscillation also generates resistive losses, which are minimized by locating the capacitor close to the sensing coil. The resonance circuit is supplied with AC to maintain the oscillation between the capacitor and the sensing coil.

The resonance frequency f_{RC} of ideal resonance circuit, meaning that resistive losses of the circuit are omitted, is determined according to

$$f_{RC} = \frac{1}{2\pi\sqrt{L_{RC}C_{RC}}} \tag{1}$$

where, L_{RC} is the equivalent inductance and C_{RC} is the capacitance of the resonance circuit (Ida, 2013). Practically, resonance circuits are non-ideal and have resistive losses. The resonance frequency which takes these losses into account can be calculated with

$$f_{RC} = \frac{1}{2\pi\sqrt{L_{RC}C_{RC}}}\sqrt{1-\frac{C_{RC}R_{RC}^2}{L_{RC}}} \tag{2}$$

where R_{RC} is a resistance of the resonance circuit. Hence, the resonance occurs only if conditions

$$\frac{C_{RC}R_{RC}^2}{L_{RC}} < 1 \quad \text{or} \quad R_{RC} < \sqrt{\frac{L_{RC}}{C_{RC}}} \tag{3}$$

are fulfilled (Wang, 2005).

Usually, C_{RC} comprises only the capacitance of the capacitor in parallel with the sensing coil and it can be assumed to be constant. Hence, f_{RC} is inversely proportional to the square root of L_{RC} that depends on the inductance of the sensing coil which changes based on surrounding materials. Therefore, the change in resonance frequency corresponds to the change in the proximity of sensed target. Figure 1 illustrates f_{RC} as a function of L_{RC}. As the frequency decreases exponentially, the resolution of the

inductive sensor decreases as a function of proximity to the measured target. Hence, inductive sensors are commonly used to measure either the presence of an object or the distance in a close range as the resolution is better on the steep and more linear part of the curve. For common commercial inductive sensors, measurement range is between $0{,}1$ and 15 mm while the resolution is approximately 2 nm (Wilson, 2004).

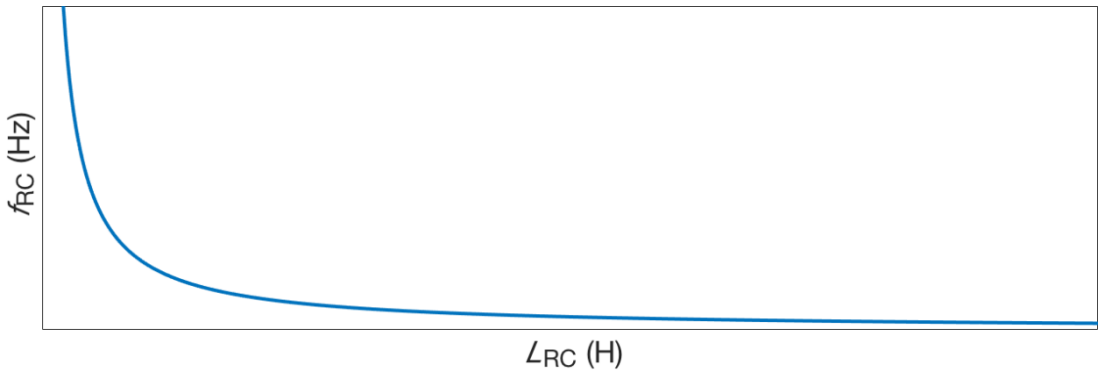

Figure 1: resonance frequency f_{RC} as a function of inductance of the sensing coil L_{RC}.

Next, the relation between the inductance and different materials is described. Generally, the inductance of a coil is defined as

$$L = \frac{N\Phi}{I} \tag{4}$$

where N is the number of turns, Φ is magnetic flux generated by the coil and I is current flowing through the coil. Furthermore, a flux produced by a coil which is around a magnetic circuit can be calculated with

$$\Phi = \frac{NI}{\mathcal{R}_m} \tag{5}$$

where $\mathcal{R}_m$ is the total reluctance of the magnetic circuit and is calculated with

$$\mathcal{R}_m = \frac{l}{\mu A} \tag{6}$$

where l is a length that the magnetic flux flows, A is the cross-sectional area of a surface which is perpendicular to the direction of magnetic flux and μ is the permeability of the magnetic circuit. Further, the magnetic permeability is defined as

$$\mu = \mu_0 \mu_r \tag{7}$$

where $\mu_0 = 4\pi \cdot 10^{-7}$ H/m is the vacuum permeability and μ_r is the relative permeability (Ida, 2013).

Figure 2 illustrates a simple approximation of a behavior of a coil which generates magnetic flux Φ to an ambient air. In this approximation, it is assumed that the magnetic flux Φ flows a certain path which length is l_m and the cross-sectional area A_m of a surface perpendicular to a direction of the magnetic flux Φ is constant throughout the whole path. Based on this approximation the inductance L_1 of this coil can be calculated by combining (4), (5), (6) and (7) as follows

$$L_1 = \frac{\mu_{ra}\mu_0 A_m N^2}{l_m} \tag{8}$$

where μ_{ra} is the relative permeability of ambient air.

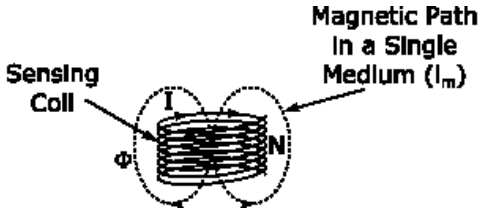

Figure 2: magnetic circuit in a single medium illustrating the variation of inductance without eddy currents.

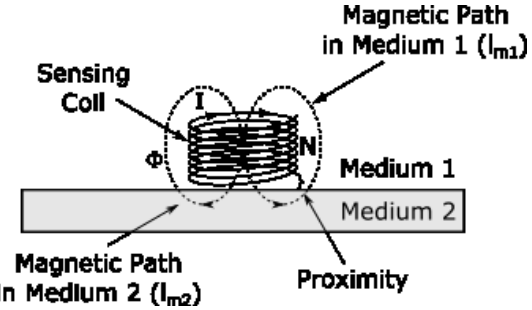

Figure 3: magnetic circuit in proximity to a second medium illustrating the variation of inductance without eddy currents.

In Figure 3 a magnetically conductive object is close to the coil of Figure 2 and a part of the magnetic flux Φ flows through this magnetically conductive object. Now, it is assumed that the magnetically conductive object does not change the path of the magnetic flux Φ illustrated in Figure 2 and that the cross-sectional area A_m of the surface perpendicular to the direction of the magnetic flux Φ is still constant throughout the whole path. Hence, the length that the generated magnetic flux Φ flows in the air is l_{m1} and the length that it flows in the magnetically conductive object is l_{m2}. With these assumptions, the inductance L_2 of the coil is

$$L_2 = \frac{\mu_{rm} l_{m1} + \mu_{rm} l_{m2}}{\mu_{rm} l_{m1} + \mu_{ra} l_{m2}} L_1 \quad (9)$$

where μ_{rm} is the relative permeability of the magnetically conductive object. Because relative permeability for magnetically conductive material is higher than for the air, the inductance L_2 of the coil close to the magnetically conductive object is higher than the inductance L_1.

In practice, the inductance of a coil cannot be calculated with (8) and (9) because of previous assumptions. However, this simplified approximation illustrated the increasing inductance of a coil when a magnetically conductive object is brought close to it. Hence, in case of inductive sensors, the resonance frequency of the sensing coil decreases as a magnetically conductive object approaches its magnetic field according to (2). Hence, inductive sensors can measure proximity even though the measured target does not conduct eddy currents.

2.2 Rotor Position Sensing in Maglev Trains

Inductive rotor position or shaft position sensing is used for radial and linear motors (Eidenvall & Linder, 2003; Hollis, Ish-Shalom, & Yarmchuk, 1995; Hosek, 2013; Yuichi & Tetsuji, 2013). However, the rotor position sensing in Maglev trains appears to be most relevant for the target of application in this thesis. Therefore, a relevant rotor position sensing solution applied to Maglev trains is studied more thoroughly in this chapter.

Generally, Maglev train comprises several carriages and each of them consists of at least one mover of a linear motor. These movers travel above a single stator rail which covers whole operation range of the Maglev train. The stator rail comprises salient teeth and is manufactured from laminated sheets of steel. The basic concept for high-speed Maglev train topology is that the train does not make contact with the stator rail while it travels at a nominal velocity. Hence, it must be simultaneously controlled to levitate above and move along the stator rail. This requires accurate and fast air gap and rotor position sensing (Steimel, 2008). In Figure 4a a basic concept of high speed Maglev train is disclosed.

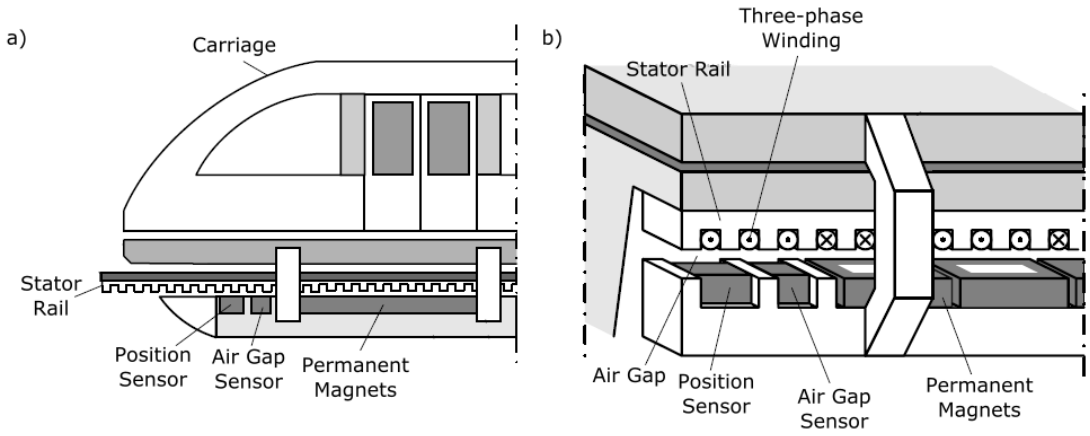

Figure 4: a) basic concept of a high-speed Maglev train. b) enlarged figure of the air gap. Modified figure from (Song, Zhiqiang, Ning, & Wensen, 2012a).

Recent publication (Song, Chunhui, & Zhiqiang, 2010) disclose a novel inductive rotor position sensor for Maglev trains. Next its basic operation principle is studied further. This rotor position sensor is located next to the stator rail and it comprises four resonance circuits. Each of these resonance circuits are used for inductive sensing. When the rotor position sensor moves along the stator rail with a constant air gap between it and the stator rail, an equivalent inductance of each resonance circuit vary periodically because the teeth of the stator rail move in relation to the resonance circuits. By demodulating and filtering the measured inductance of the resonance circuits, four approximately sinusoidal inductance signals are obtained. Finally, the position of the Maglev train is determined with these signals.

While the rotor position sensor travels above the stator rail, each resonance circuit provides inductance measurement results which form four sinusoidal inductance signals as mentioned. The rotor position sensing from a separate inductance signal is difficult because a difference between consecutive inductance measurement results near the top and bottom of the sinusoidal signal is much less than on the slopes between them. Therefore, in those areas the measurement error increases. To prevent this, the Maglev rotor position sensor utilizes several inductance signals and determines the position only according to measurement results that have been measured from the slopes.

In the Maglev train application, the stator tooth is equal to the stator slot. The length of one stator tooth and slot is later referred as a pole pitch l_{PP} Figure 5 shows the

arrangement of the resonance circuits in the Maglev train rotor position sensor. Resonance circuit groups 1 and 2 in Figure 5 have a displacement of $0{,}25l_{PP}$. The length of each resonance circuit along the stator rail is equal $0{,}5l_{PP}$ meaning that both groups cover the length of l_{PP}. The width of each resonance circuit is half of the stator rail width meaning that the area of the resonance circuits above the stator rail is maximized. This is done because measured signal intensity increases with the size of the resonance circuit (Song et al., 2010).

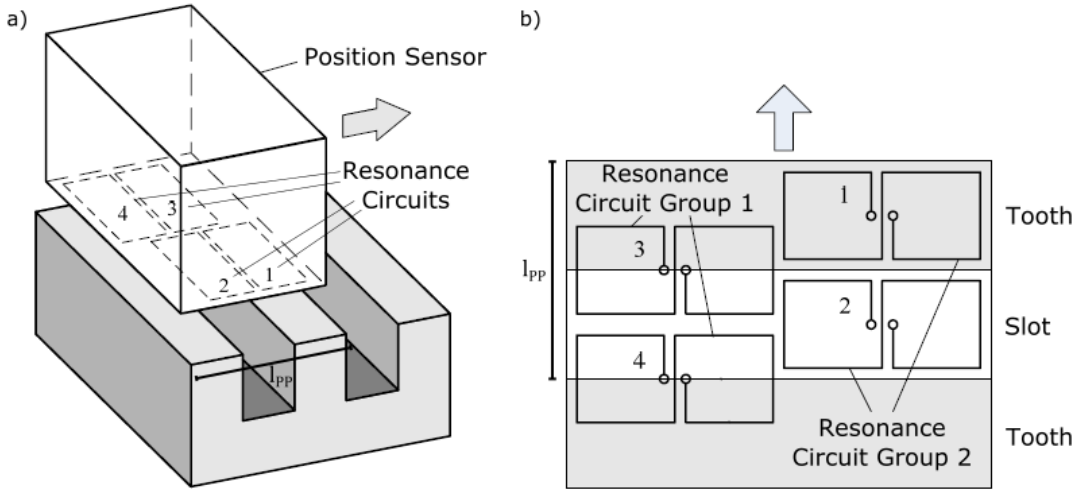

Figure 5: a) inductive rotor position sensor used for Maglev train rotor position sensing. b) arrangement of resonance circuit groups within the rotor position sensor (Song et al., 2012a).

Because of the resonance circuit arrangement, the sinusoidal inductance signals from resonance circuits within the same group have $180°$ phase shift and the groups have $90°$ phase shift meaning that resonance circuits 1 and 3 in Figure 5 generate signals with $90°$ phase shift. Respectively, resonance circuits 2 and 4 generate signals with $90°$ phase shift. Two sinusoidal difference signals D_1 and D_2, one for each resonance circuit group, are generated from the sinusoidal inductance signals of the resonance circuits 1-4. The difference signal D_1 is generated by subtracting the inductance signal of resonance circuit 4 from the inductance signal of resonance circuit 3 (Song et al., 2012a). Respectively, D_2 is generated by subtracting inductance signal from resonance circuit 2 from inductance signal of resonance circuit 1.

Hence, the difference signals have same frequency and double the peak-to-peak amplitude of the original signals they are generated from. Also, D_1 and D_2 have $90°$ phase shift. The use of difference signals instead of the inductance signals of the resonance circuits 1-4 eliminates common mode disturbances e.g. temperature drift.

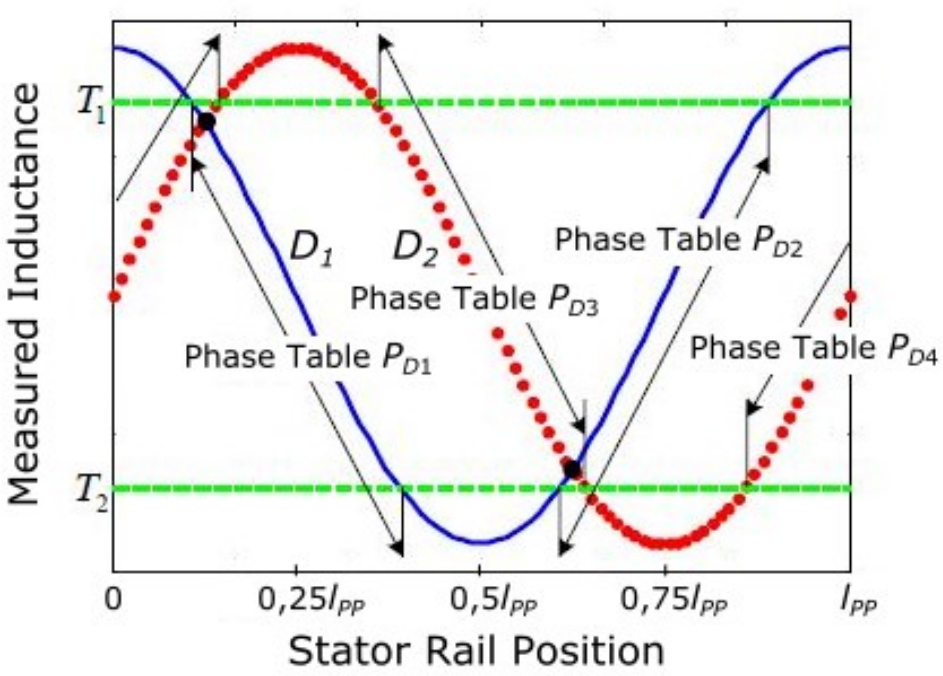

Figure 6: look-up table method including difference signals D_1 (blue), D_2 (red) and phase tables $P_{D1} - P_{D4}$. This figure is modified from (Song et al., 2012a).

A look-up table method is used to determine the rotor position from the difference signals D_1 and D_2 (Song, Ning, & Zhiqiang, 2012b; Song et al., 2012a). In the method, threshold limits T_1 and T_2 are determined for the difference signals D_1 and D_2. The threshold values are determined such that the slopes of the difference signals D_1 and D_2 between T_1 and T_2, are linear. Also, the look-up table method comprises phase tables P_{D1}, P_{D2}, P_{D3} and P_{D4} which include a corresponding stator rail rotor position for difference signal values between the threshold limits T_1 and T_2. To determine the rotor position, a value of the difference signal D_1 or D_2 is compared to a corresponding phase table. Phase tables and difference signals generated from the distance of stator rail pole pitch shown in Figure 6. The rotor position, in the case of Figure 6, is determined by comparing the value of difference signal D_1 to phase table P_{D1}. When the value of difference signal D_1 goes below T_2 the rotor position is

determined by switching to compare difference signal D_2 to phase table P_{D3}. Respectively, when the value of the difference signal D_2 exceeds threshold limit T_1 the rotor position is determined by comparing D_1 to P_{D2}. Hence, difference signal and phase table under comparison are changed when the difference signal value exceeds T_1 or goes below T_2. Table 1 shows which difference signal and phase table are under comparison at a time and which are selected to be compared next if the value of the difference signal goes out of an interval $[T_1, T_2]$.

Table 1: look-up table defining which difference signal and phase table are under comparison at a time. This table is modified from (Song et al., 2012a).

Current difference signal and phase table	**Condition to switch difference signal and phase table**	**Next difference signal and phase table**
D_1 & P_{D1} or D_2 & P_{D2}	$D_1 > T_1$	Phase table 4
	$D_1 < T_2$	Phase table 3
D_3 & P_{D3} or D_4 & P_{D4}	$D_2 > T_1$	Phase table 1
	$D_2 < T_2$	Phase table 2

This inductive rotor position sensor and look-up table method was tested with a Maglev train at $1{,}5$ km long test line in Shanghai. The inductive rotor position sensor and the look-up table method performed well during these test runs (Song et al., 2012a).

3 Application Environment

In this chapter, the application is described. Then, the requirements for the sensing apparatus are defined.

3.1 General Overview

The sensing apparatus is developed for a mover which consists of two permanent magnet linear motors. Both PMLMs have their own permanent magnets, multi-phase winding around an iron core, primary, and they are operated with individual frequency converters that are controlled by a controller. The mover travels along a linear stator rail, secondary, and it is installed in a way that the stator penetrates the mover as in Figure 7 (Purosto, Hakala, Ratia, & Petrov, 2016). PMLMs locate on opposite sides of the stator rail, forming an air gap between PMLMs and the stator rail. The mover is not attached or bearing-mounted to the stator rail by any means. Hence, in absence of control the mover comes into contact with a surface of the stator rail because of a force generated by the permanent magnets.

The stator rail comprises two magnetic circuits which are located on opposite sides of a supporting structure. The supporting structure is magnetically non-conductive; however, it conducts electricity. The magnetic circuits are manufactured from laminated sheets of steel and they comprise salient teeth pointing towards the air gap. A magnetic field is generated in the mover windings, producing magnetic flux which flows from the primary, through the air gap, to the teeth of the secondary. On the secondary side, the magnetic flux flows via adjacent teeth and the air gap back to the primary, closing the magnetic circuit. The controller controls frequency converters to supply alternating currents to the mover windings, generating motion with a changing magnetic field. Respectively a force towards the stator rail is controlled by changing the intensity of magnetization in the mover windings.

The stator rail is covered with a coating that is magnetically and electrically non-conductive. This coating fills the stator rail slots and covers the teeth with a thin layer.

Hence the stator is a continuous straight rail with a flat surface. Therefore, a contact between mover and the stator rail does not cause significant damage to the mover.

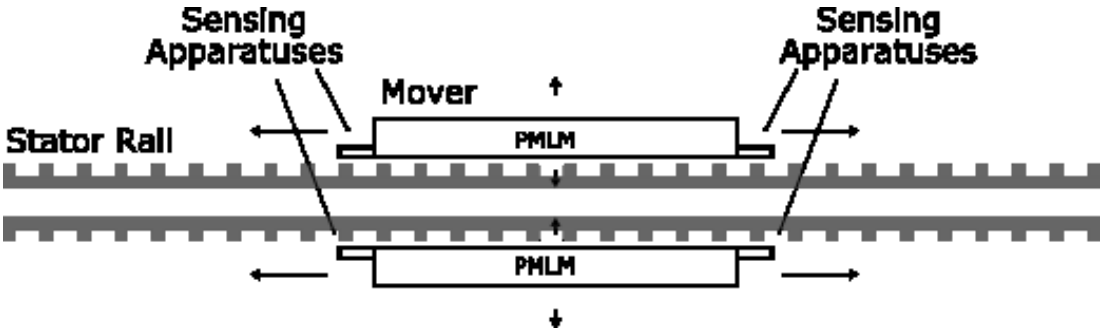

Figure 7: mover comprising a permanent magnet linear motor on each side of the linear double-sided stator.

Basically, the mover levitates constantly and requires active control or the force of the permanent magnets drive one of the air gaps to zero preventing the motion along the stator rail. The nominal air gap in this application is $1{,}25$ mm meaning that on both sides of the stator rail, the air gap varies from 0 to $2{,}5$ mm. Although, previously mentioned coating prevents significant damages, the contact between stator rail and the mover is not desirable while the mover is travelling. Hence, the control comprises simultaneous levitation and motion control.

The ratio of teeth to slots is 1:2 in the stator rail. The stator rail and the supporting structure are shown in Figure 8. The length of a tooth $l_T = 10$ mm, the height of a tooth $l_H = 8$ mm and the width of the slot $l_S = 20$ mm. Additionally, the width of the magnetic circuit in the stator rail $l_W = 54$ mm. Pole pitch $l_{PP} = l_T + l_S = 30$ mm.

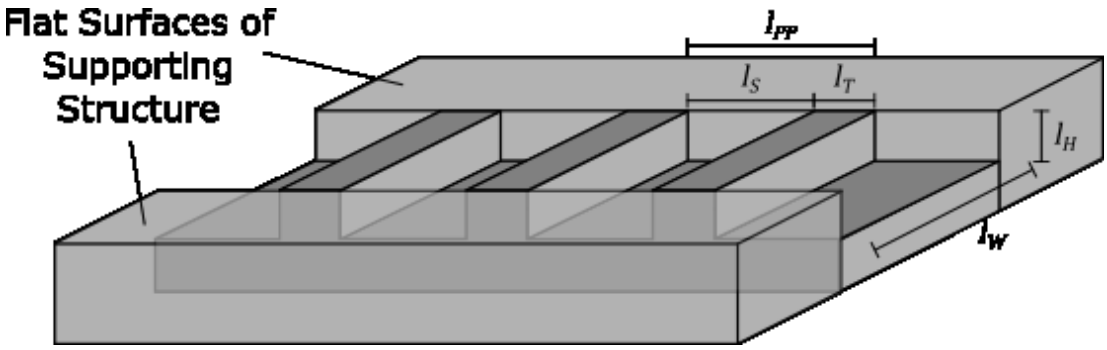

Figure 8: stator rail and symbols representing the dimensions.

3.2 Requirements for the Sensing Apparatus

The purpose of the sensing apparatus is to measure the air gap and position of the mover and provide the measurement results to the controller. The measurement time and accuracy must be such that the controller is able to provide motion and levitation control for the frequency converters of the mover. This control comprises a generation of pulse-width modulated (PWM) control signals for the inverter switches of the frequency controllers to supply current for the PMLMs of the mover. Hence, the generation time of the PWM control signals, switching frequency of the frequency controllers and the measurement time of the sensing apparatus are limiting factors for the levitation and motion control.

The current supplied to the PMLMs is controlled by controlling the mean value of voltage across the PMLM windings. This is done by controlling the duty cycle the PWM control signals. The duty cycle is the ratio between the time of conducting switch state and the switching period T_{sw}. During the switching period, the controller generates new PWM control signals for the next switching period. Therefore, control cannot be changed before next switching period T_{sw} starts.

New PWM control signals are generated according to the air gap and rotor position sensing results. Therefore, the measurement time of the sensing apparatus t_M, meaning the time between the start of a measurement and the moment the measurement result is provided to the sensing apparatus output, should be such that the controller can provide smooth motion control for the mover. In case the measurement time t_M is more than the switching period T_{sw}, the controller generates new PWM control signals according to previous air gap and rotor position sensing results which is not desirable in this application. The switching time of the inverter switches is 50 µs. As the control can be changed only at intervals of the switching period T_{sw} which is longer than the switching time of the inverters, the measurement time requirement t_M is set to be more than 50 µs. Generally, the faster the measurement results are available the better from the control point of view. However, this minimum limit is set because decreasing measurement time t_M too much can decrease the resolution. Hence if the sensing apparatus appears to reach lower measurement time t_M, the sensing apparatus design

will be changed to improve sensing resolution at cost of the measurement time t_M.

In this application, the resolution of the mover position should be less than 83 µm to provide a smooth motion control for the mover. This should be feasible with $2{,}5$ mm air gap because Maglev train rotor position sensor reached similar resolution with 8 mm air gap (Ning, Song, Zhiqiang, & Jingnan, 2012). Additionally, the measurement time t_M should be such that when the mover travels along the stator rail with a maximum velocity, the distance between two consecutive measurements l_M is less than 83 µm. The measurement time t_M is calculated with

$$t_M = \frac{l_M}{v_m} \tag{10}$$

where v_m is the velocity of the mover. According to (10) and with initial values $l_M \leq 83$ µm and $v_m = 1$ m/s, a requirement $t_M \leq 83$ µs in the rotor position sensing is defined.

The levitation control requires air gap sensing resolution to be less than 10 µm. Furthermore, the time of driving the mover air gap from 0 to $2{,}5$ mm, i.e. from one side of the stator rail to the other, is 30 ms. Hence, according to (10), a requirement $t_M \leq 120$ µs in the air gap sensing is defined.

The design is such that one sensing apparatus is attached to both ends of the mover. This allows to measure inclination of the mover which is necessary in the levitation control. The sensing apparatus is required to be rigidly attachable to the ends of the mover. This prevents measurement errors caused by bending and vibration. Therefore, the maximum width and height of the sensing apparatus are required to be at most equal to width and height of the mover.

As a summary, the air gap and rotor position sensing requirements that the sensing apparatus should fulfil are collected in Table 2.

Table 2: requirements for the sensing apparatus.

Requirement	**Resolution [µm]**	$\boldsymbol{t_M}$ **[µs]**
Air gap	≤ 10	$50 \leq t_M < 120$
Position	≤ 83	$50 \leq t_M < 83$

4 Design of the Sensing Apparatus

In this chapter, the basis of the sensing apparatus design is introduced. Then the air gap and rotor position sensing functionalities are discussed separately. Finally, a manufactured prototype of the sensing apparatus is described.

4.1 Basis of the Design

The Maglev train rotor position sensing solution with inductive sensors is selected for the basis of the sensing apparatus design because it is similar application and proven to work (Song et al., 2012a). It has promising features like the relatively cheap price of inductive sensors, possibility to design the sensing apparatus to a single printed circuit board (PCB) and sensing through electrically and magnetically non-conductive materials, which suits especially well for dirty environments (Wilson, 2004). Also, as this rotor position sensing solution is suitable for operating at Maglev train velocities and fulfils strict safety regulations related to the means of public transportation, it should be sufficient for this application.

The Maglev train rotor position sensing solution is developed for a stator rail which ratio of teeth to slots is 1:1. Therefore, the solution should be further developed and tested to suit the ratio of 1:2 in this application. Especially, accuracy and the measurement time should be tested to verify that inductive sensors can be used for air gap and rotor position sensing in this application.

An analog-to-digital (A/D) converter, LDC1101 from Texas Instruments and later referred as A/D converter, is selected to be the inductive sensor for the sensing apparatus. According to the manufacturer, it is a high-resolution, high-speed inductance-to-digital converter and its typical applications are e.g. high-speed gear counting, high speed event counting, motor speed sensing, motor control and metal detection, with sub-micron measurement resolution (Texas Instruments, 2015). The size of the A/D converter is rather small ($3{,}1$ mm $\cdot 3{,}1$ mm $\cdot 1$ mm) and it can measure up to $180\ 000$ samples per second. The A/D converter is used with an external resonance circuit and its unit price is a few euros.

A previous version of the A/D converter, LDC1000, was tested with similar PCB resonance circuits and results appeared promising (Zuk, Pietrikova, & Vehec, 2016). According to A/D converter datasheets, the LDC1101 should perform better than LDC1000 in this application. As a conclusion, the sensing apparatus is designed to be an inductive sensor on a PCB based on the Maglev train rotor position sensing solution. The prototype is designed and manufactured with LDC1101 A/D converters.

4.2 Rotor Position Sensing

Rotor position sensing of the sensing apparatus is based on the Maglev train solution with following modifications. Six position sensing resonance circuits are used instead of four and their shapes and arrangement is different. Furthermore, six difference signals are generated from position sensing resonance circuit output signals and with threshold limits T_1 and T_2, six phase tables are generated from these difference signals.

The sensing apparatus design differs from the Maglev train solution by having three sensing coils in both sensing coil groups instead of two. Six position sensing resonance circuits are used because the ratio of teeth to slots in the stator rail is 1:2 instead of 1:1. If only four position sensing resonance circuits were used to determine mover position, occasionally they all would locate simultaneously above a stator rail slot. This would make rotor position sensing impossible with the look-up table method. Figure 9 show the arrangement of sensing coils above the stator rail.

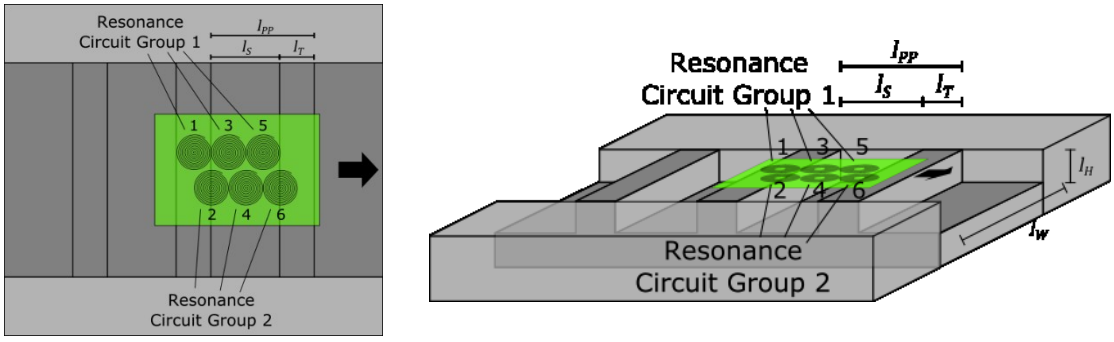

Figure 9: arrangement of position sensing resonance circuits 1 – 6 above the stator rail.

Due to the ratio of 1:2, output signals of position sensing resonance circuits cannot be approximated sinusoidal. Instead, the position sensing resonance circuit output signal comprises two parts. First part can be approximated to a half wavelength of a sine wave, starting from its highest point. This part is an output signal of a position sensing resonance circuit traveling over a stator tooth. For example, S_6 between 0 and $0{,}66\ l_{PP}$ in Figure 10 illustrates the output signal when the first resonance circuit is above a stator tooth. The latter part of a position sensing resonance circuit output signal is constant as the resonance circuit travels above a stator rail slot (e.g. S_6 between $0{,}66$ and $1{,}0l_{PP}$). When a position sensing resonance circuit reaches next stator rail tooth (e.g. S_6 at $1{,}0l_{PP}$), the output signal starts over. Approximated position sensing resonance circuit output signals $S_1, S_2, \dots, S_6$ are shown in Figure 10. In this approximation, the velocity and the air gap of the mover is constant.

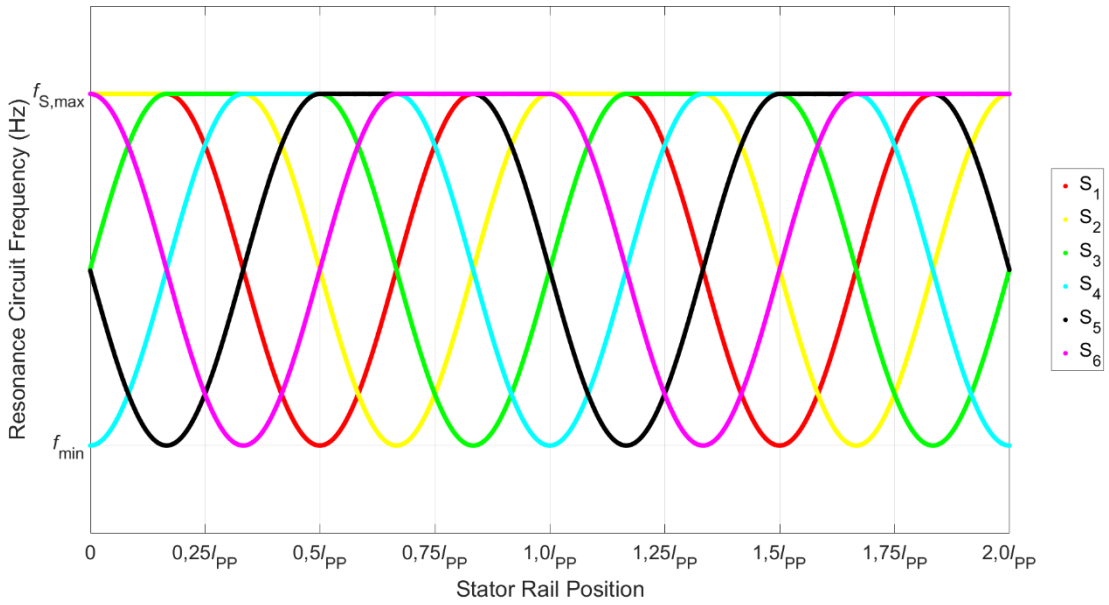

Figure 10: approximated position sensing resonance circuit output signals from the distance of two pole pitches. The lowest frequency of the resonance circuit output signals is marked in the figure as f_{min} and the highest is marked as $f_{S,max}$. The velocity and the air gap of the sensing apparatus are constant in this approximation.

Like the Maglev train solution, difference signals $D_1, D_2, \dots, D_6$ are generated by subtracting position sensing resonance circuit output signals within each group. Equations for generating difference signals are shown in Table 3. These difference

signals are output signals of the sensing apparatus. Figure 11 shows difference signals, which are generated from the position sensing resonance circuit output signals of Figure 10.

Table 3: generation of difference signals.

	Difference signal		
Group 1	$D_1 = S_1 - S_3$	$D_3 = S_3 - S_5$	$D_5 = S_5 - S_1$
Group 2	$D_2 = S_2 - S_4$	$D_4 = S_4 - S_6$	$D_6 = S_6 - S_2$

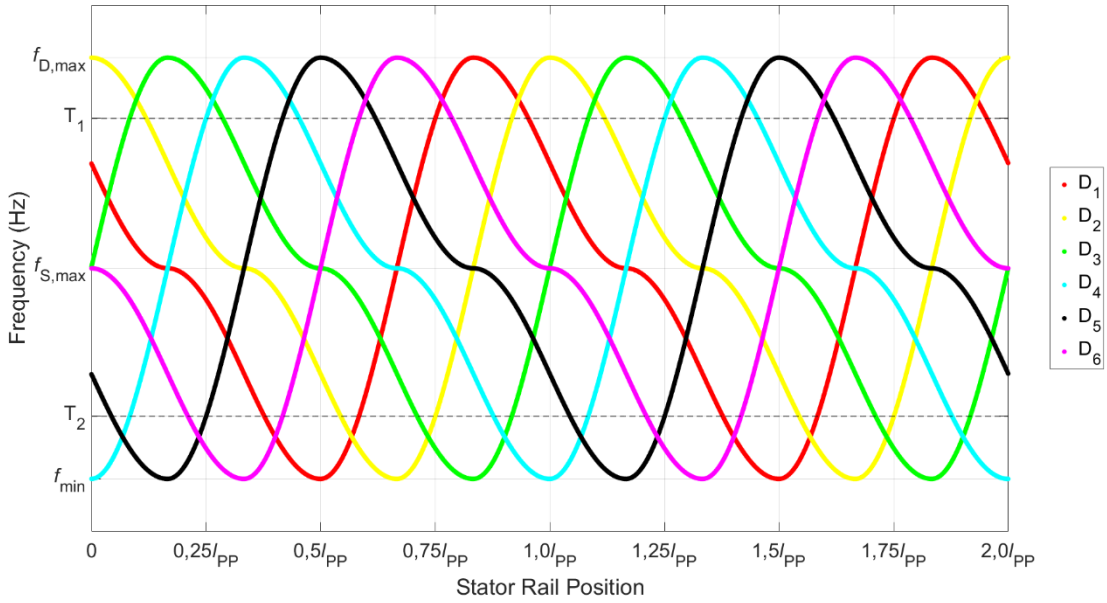

Figure 11: difference signals generated from the approximated position sensing resonance circuit output signals shown in Figure 10. The lowest frequency of the difference signals is marked in the figure as f_{min} and the highest is marked as $f_{D,max}$. The maximum frequency of the approximated position sensing resonance circuit output signals, with an assumption that they have common f_{min}, is marked in the figure as $f_{S,max}$ to illustrate the amplitude of difference signals.

Values between T_1 and T_2 on the rising slope of difference signals $D_1, D_2, \dots, D_6$ are stored to phase tables $P_{D1}, P_{D2}, \dots, P_{D6}$. Additionally, phase tables include rotor position information for each value stored to the phase table. The equations for generating the phase tables from the rising slopes are shown in Table 4. Figure 12 shows phase tables, which are generated from the difference signals of Figure 11.

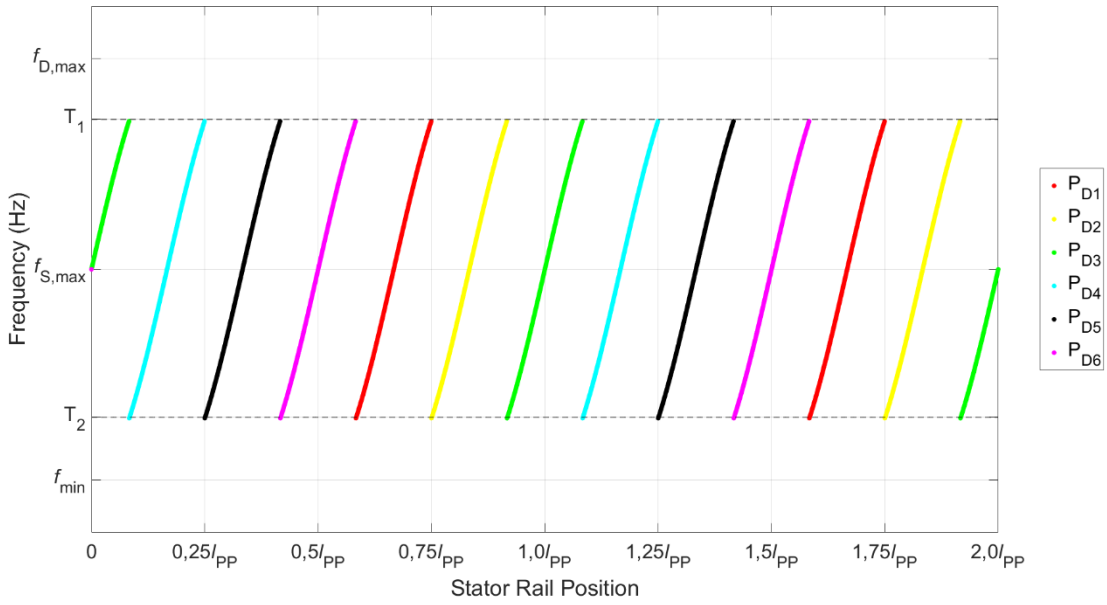

Figure 12: phase tables generated from the difference signals shown in Figure 11.

Table 4: generation of phase tables from the rising slopes of difference signals.

Phase table
$P_{D1} = \{x \in D_1 : T_1 \leq x \leq T_2\}$
$P_{D2} = \{x \in D_2 : T_1 \leq x \leq T_2\}$
$P_{D3} = \{x \in D_3 : T_1 \leq x \leq T_2\}$
$P_{D4} = \{x \in D_4 : T_1 \leq x \leq T_2\}$
$P_{D5} = \{x \in D_5 : T_1 \leq x \leq T_2\}$
$P_{D6} = \{x \in D_6 : T_1 \leq x \leq T_2\}$

The phase tables are stored to a non-volatile memory of the controller which determines rotor position by comparing difference signal values of the sensing apparatus output to corresponding phase tables. The controller selects always the difference signal which is on its rising slope to be compared to corresponding phase table. The compared difference signal and phase table are switched to next ones if difference signal value is above T_1 i.e. exceeds phase table values. Respectively previous difference signal and phase table are selected if difference signal value goes below T_2. Table 5 shows which difference signal and phase table are compared and which are selected if difference signal value goes out of an interval $[T_1, T_2]$.

Table 5: look-up table for a controller to define which difference signal and phase table are under comparison at a time.

Current difference signal and phase table	**Condition to switch difference signal and phase table**	**Next difference signal and phase table**
D_1 & P_{D1}	$D_1 > T_1$ $D_1 < T_2$	D_2 & P_{D2} D_6 & P_{D6}
D_2 & P_{D2}	$D_2 > T_1$ $D_2 < T_2$	D_3 & P_{D3} D_1 & P_{D1}
D_3 & P_{D3}	$D_3 > T_1$ $D_3 < T_2$	D_4 & P_{D4} D_2 & P_{D2}
D_4 & P_{D4}	$D_4 > T_1$ $D_4 < T_2$	D_5 & P_{D5} D_3 & P_{D3}
D_5 & P_{D5}	$D_5 > T_1$ $D_5 < T_2$	D_6 & P_{D6} D_4 & P_{D4}
D_6 & P_{D6}	$D_6 > T_1$ $D_6 < T_2$	D_1 & P_{D1} D_5 & P_{D5}

As an example, if the sensing apparatus outputs $D_5 = T_2$, a controller compares D_5 to P_{D5} which results rotor position of $0{,}25 l_{PP}$ according to Figure 12. When $D_5 = T_1$, resulting rotor position of $0{,}44 l_{PP}$, a controller determines that a mover has travelled $5{,}83$ mm along the stator rail. Further, when $D_5 > T_1$ a controller switches to compare D_6 to P_{D6}. When $D_6 = f_{S,max}$, a controller determines that the rotor position is $0{,}5 l_{PP}$ and therefore mover has travelled another $1{,}67$ mm.

4.3 Air Gap Sensing

The supporting structure of the stator rail comprises flat surfaces on both sides of the stator rail, covering its whole length. This surface is electrically conductive and therefore a resonance circuit can measure proximity from it. The sensing apparatus design comprises two air gap sensing resonance circuits that locate above the flat surfaces.

They are used to measure the air gap and angle of the mover. Figure 13 shows the air gap sensing resonance circuits 7 and 8 on both sides of position sensing resonance circuits.

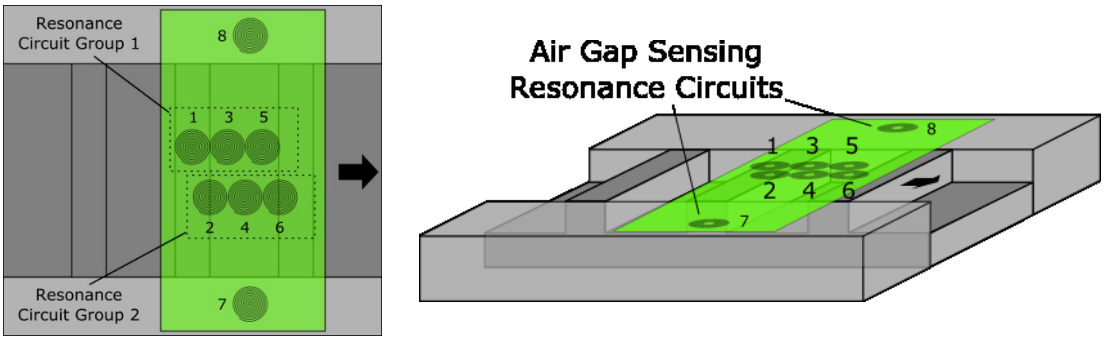

Figure 13: arrangement of position and air gap sensing resonance circuits above the stator rail. The air gap sensing resonance circuits 7 and 8 measure the air gap from the flat surface of an electrically conductive supporting structure.

A design requirement for the air gap sensing resonance circuits 7 and 8 in Figure 13 is that their sensing range does not extend to cover the stator rail. Otherwise, the teeth of the stator rail within the sensing range would cause measurement errors. Therefore, one possible shape for the air gap sensing resonance circuits could be a long and narrow multi-layer coil that is longer than one pole pitch. That shape should decrease the measurement error, in case the sensing range extended to cover the stator rail.

4.4 Design of the Sensing Apparatus Prototype

The sensing apparatus prototype comprises two PCBs which are connected with a cable. One PCB comprises most of the electronics and is later referred as electronics printed circuit board (EPCB). The other, later referred as a sensor printed circuit board (SPCB), comprises resonance circuits. The division into two separate PCBs allows to test different SPCB designs with same electronics.

The prototype design comprises six position sensing resonance circuits without air gap sensing resonance circuits. Hence, rotor position sensing can be tested using one or more position sensing resonance circuits above the stator rail and the air gap sensing

can be tested using the same position sensing resonance circuits above the flat surface of the supporting structure.

Resonance circuits on SPCBs are designed using capacitors connected in parallel with circular, square, hexagonal or octagonal sensing coils. Despite of the sensing coil shape, its diameter is the tooth length l_T. Only similar sensing coils are used within a single SPCB and therefore four different SPCBs are designed. Compared to the rotor position sensing design in Figure 9, the position sensing resonance circuits on SPCBs are located further apart each other to minimize interference. The position sensing resonance circuit groups are moved further from the center of the stator rail and the middle resonance circuits from both groups are moved close to the sides of the stator rail as is shown in Figure 14. Because the relative location of the resonance circuits along the stator rail does not change, the position sensing resonance circuit output signals, generated difference signals and phase tables remain the same.

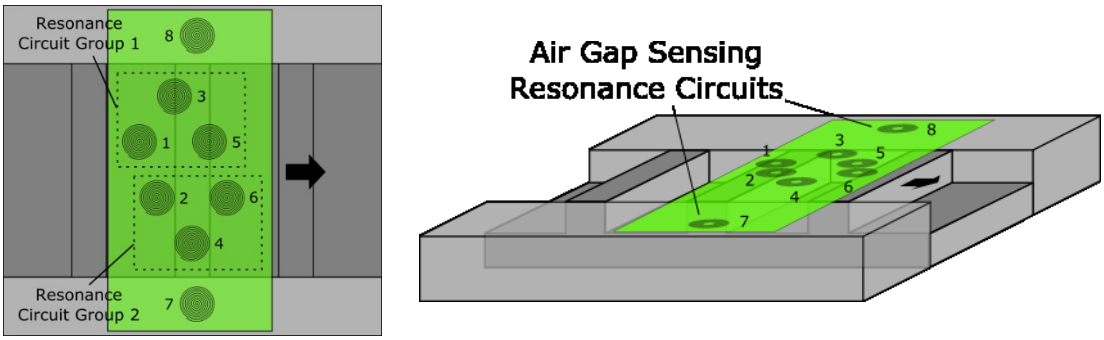

Figure 14: arrangement of position and air gap sensing resonance circuits above the stator rail. The position sensing resonance circuit arrangement within resonance circuit groups are shown.

In addition to the position sensing resonance circuit dimensions and shapes, the main SPCB design parameters are the inductance, quality factor and operating frequency of the resonance circuits (Ning, Zhiqiang, Song, & Fengshan, 2013). The SPCB designs are shown in Figure 15.

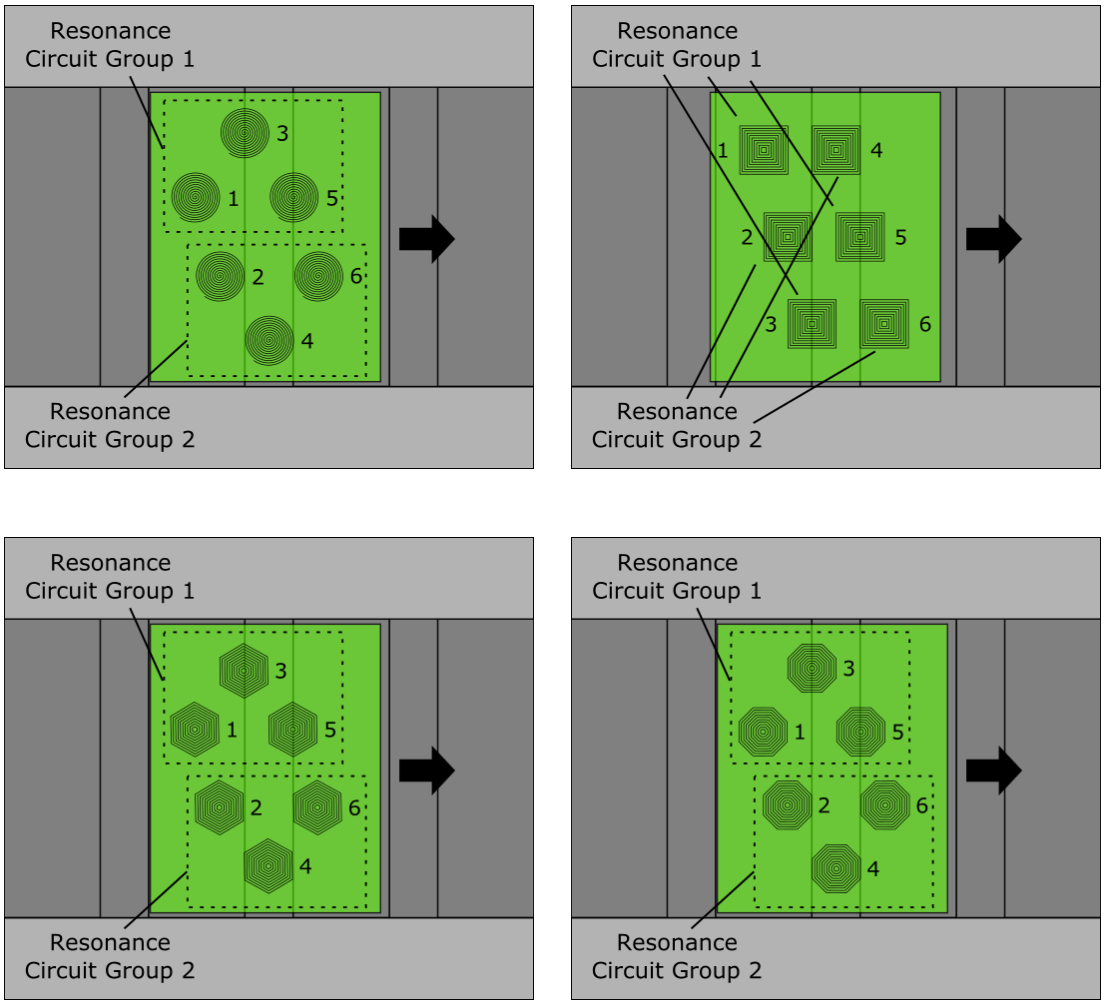

Figure 15: SPCB designs for manufacturing.

Eight SPCBs were manufactured and the four having $1{,}5$ MHz operating frequency are shown in Figure 16. The width of each manufactured SPCB is 54 mm which is the same as the width of the stator rail l_W. The length of the SPCBs is $47{,}1$ mm.

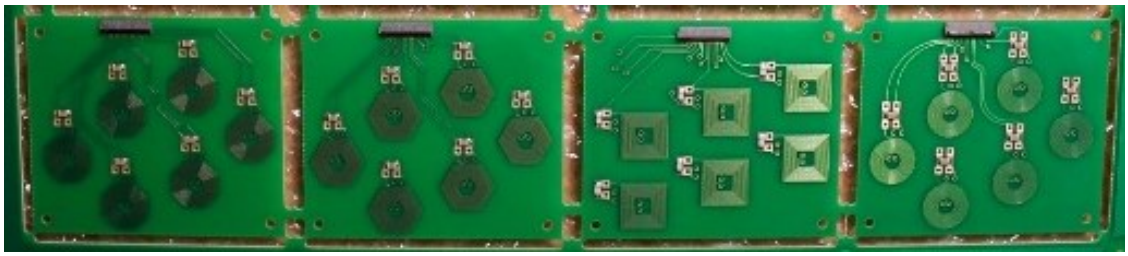

Figure 16: manufactured SPCBs.

These designs with different operating frequencies are manufactured for the sensing apparatus prototype. The operating frequencies of the SPCBs are set with the number

of turns in the resonance circuits and with the capacitor values. Specific information about the designed SPCBs are shown in Table 6.

Table 6: properties of manufactured SPCBs.

Sensing coil shape	PCB layers	Turns	Operating frequency [MHz]	Inductance [µH]	Quality factor	Capacitance [pF]
Circular	4	8	3,3	5,699	45,80	390
Circular	4	11	1,5	11,52	26,04	1000
Square	4	8	3,3	6,797	54,39	330
Square	4	11	1.5	13,74	31,35	820
Hexagonal	4	8	3,3	5,796	46,27	390
Hexagonal	4	11	1,5	11,68	26,25	1000
Octagonal	4	8	3,3	5,833	46,44	390
Octagonal	4	11	1,5	11,77	26,37	1000

As mentioned, the design of EPCB is based on LDC1101 A/D converters. EPCB comprises six A/D converters which can be connected to external resonance circuits on SPCBs. Therefore, each A/D converter is measuring the inductance of a separate resonance circuit. In addition to A/D converters, EPCB comprises a buck converter, reference clock and passive components, which are all surface-mounted components attached to a top layer of a four-copper layer PCB. Top and bottom layers of this PCB are signal planes, lower inner layer is a power plane and upper inner layer is a ground plane. All components on EPCB are selected to have same operating voltage V_{DD}, which is supplied from the power plane.

A buck converter, Texas Instruments TSP62220, is used to regulate the power plane at the operating voltage. This converter is a DC/DC converter which output voltage can be set to a constant level with passive components. The passive components are selected such that the buck converter input voltage V_{CC} can be supplied with $3{,}6$ - 6 V DC while the output voltage V_{DD} remains at $3{,}3$ V DC. The voltage V_{CC} is supplied to EPCB input from an external power source. This buck converter is used to protect EPCB against possible voltage peaks in the EPCB input.

The A/D converter can operate in two different measurement modes. However, only the measurement mode which has higher resolution and completes measurements regularly i.e. at constant intervals, is used. In that measurement mode, the A/D converter compares the oscillation frequency of the external resonance circuit to a constant frequency of an external reference clock f_{CLKIN} and determines the inductance based on the difference.

The A/D converter supports a 4-pin serial peripheral interface (SPI) bus communication protocol. It operates as a slave in this bus and requires an external master, e.g. microcontroller, to operate. A brief introduction to the SPI communication protocol is necessary to understand the delays of the sensing apparatus prototype. SPI communication protocol is quite loose and therefore the protocol is described as it is applied for this LDC1101 A/D converter.

In the SPI protocol, a master communicates only with one slave at a time. Each slave shares a common master input slave output line (MISO), master output slave input line (MOSI) and serial clock line (SCLK). Furthermore, individual chip select bus (CSB) is provided from the master to each slave. In the beginning of a master-slave communication, the master selects the slave by switching its CSB low while the CSBs for other slaves are high. Hence, only the particular slave in the bus is allowed to send data to MISO. In master-slave communication, the master either reads or writes data to slave registers, each containing one byte of data. First the master sends a command byte to MOSI and simultaneously provides eight serial clock cycles to SCLK. The command byte comprises either a read or a write command and a slave register address. Then the master provides eight serial clock cycles to SCLK for each consecutive slave registers it intends to read or write starting from the address sent in the command byte. During that either the slave sends register values to MISO (read command) or the master sends new register values to MOSI (write command). In the end of master-slave communication CSB is set high. Hence, the master can read or write with a single command byte many consecutive slave registers. Figure 17 shows a block diagram of a single A/D converter and required connections to the master.

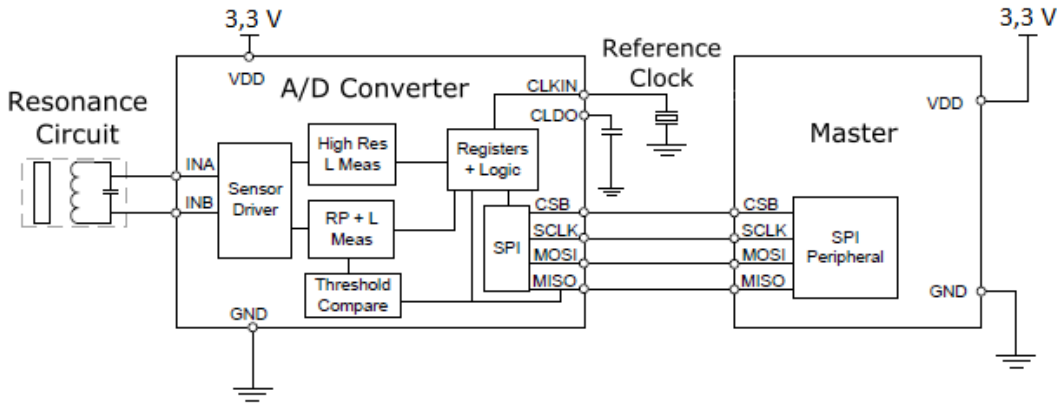

Figure 17: circuit diagram for operating LDC1101. This figure is modified from (Texas Instruments, 2015).

The EPCB is designed without a master. MOSI, MISO, SCLK and CSBs are connected to EPCB input. Therefore, any device capable of operating as a master in the SPI communication protocol can be used.

When A/D converter completes a measurement its status register changes. Therefore, the master reads the status register repeatedly until it changes. Then the master reads a measurement result from three consecutive A/D converter registers. After the measurement result has been read, status register resets and the master starts to read it again. The master-slave communication time t_{SPI} is determined with

$$t_{SPI} = \frac{8n_B}{f_{SCLK}} \tag{11}$$

where n_B is the number of communicated bytes and $f_{SCLK} = 8$ MHz is a serial clock frequency in SCLK. Hence, $t_{SPI} = 2$ µs for reading status register and $t_{SPI} = 4$ µs for reading a measurement result. Because the master starts to read the measurement result registers after the status register indicates completion of a measurement, the delay between the completion of a measurement and the moment when the master has read the measurement result varies between 4 and 6 µs.

A conversion time t_c which A/D converter requires to complete a measurement can be calculated with

$$t_c = t_{PCP} + \frac{16n_C}{f_{CLKIN}} = \frac{55 + 16n_C}{f_{CLKIN}} \tag{12}$$

where t_{PCP} is a constant post-conversion processing time and n_C is a settable A/D converter parameter which determines the number of reference clock cycles used for each measurement. According to (12), higher n_C results higher measurement resolution and longer conversion time. With n_C the conversion time can be selected between $5{,}4$ µs and $65{,}5$ ms.

Hence, total delay from the start of a measurement to the moment when the master receives the measurement result can be set between $9{,}4\ \mu s$ and $65{,}5\ ms$. These delays fulfil the air gap and rotor position sensing requirements set for the measurement time t_M. However, A/D converter manufacturer has not provided means to calculate the measurement resolution and therefore the prototype must be tested to verify that it can reach the required measurement time t_M with sufficient resolution.

The circuit diagram of the EPCB is shown in Figure 19. More information about the components in the circuit diagram is presented in Table 7. The manufactured EPCB is shown in Figure 18. The width of the manufactured EPCB is $52{,}2$ mm and the length is $39{,}1$ mm.

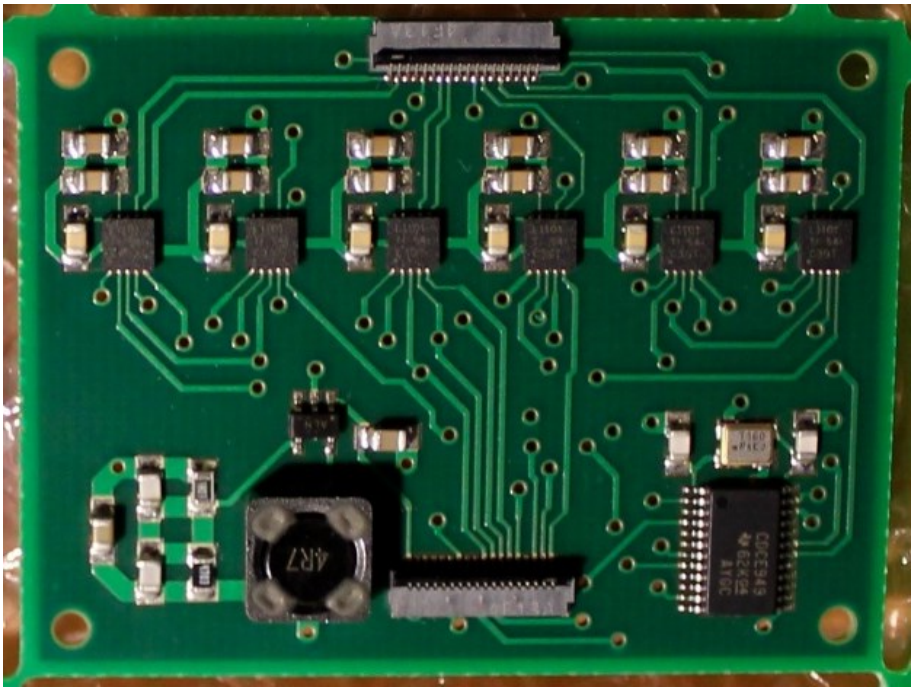

Figure 18: manufactured EPCB.

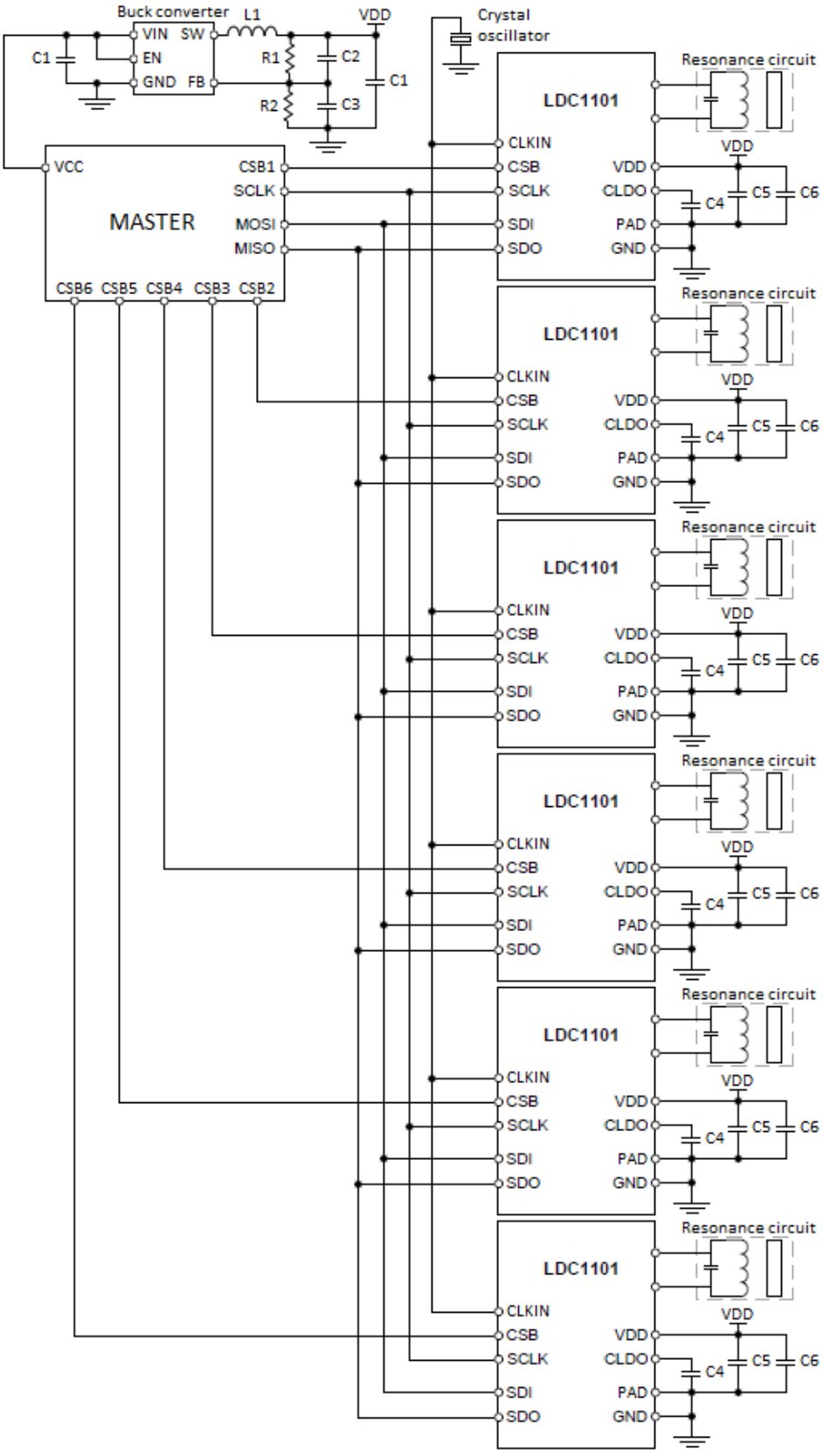

Figure 19: EPCB circuit diagram.

Table 7: component of the EPCB.

Components		**Capacitors [nF]**	**Inductor [µH]**	**Resistors [kΩ]**
A/D converter	LDC1101	$C1 = 10000$	$L1 = 10$	$R1 = 680$
Buck converter	TSP62220	$C2 = 0{,}01$		$R2 = 120$
Reference clock	16 MHz crystal oscillator	$C3 = 0{,}15$		
Master	MSP432P401R	$C4 = 15$		
		$C5 = 100$		
		$C6 = 1000$		

5 Measurements

In this chapter, a test arrangement for the sensing apparatus prototype is introduced. Then, test runs and their purposes are covered. Finally, test results are disclosed and analyzed.

5.1 Test Arrangement

The test arrangement for the prototype is developed and built to test the air gap and rotor position sensing separately. In addition to the test arrangement, the method to collect sensing apparatus measurement results is developed. Next both topics are discussed more thoroughly.

The test arrangement comprises a carrier and a 90 cm long stator rail which is attached to a framework structure. The carrier is manufactured from aluminum to be light and rigid. Furthermore, it is bearing-mounted from four corners to two parallel bars attached to the framework structure. The stator rail locates between these bars equally apart in such a way that the carrier can travel along the stator rail. The bearings are attached to the carrier with screws. The carrier is fastened to the screws with nuts, allowing to adjust the height and angle of the carrier. The test arrangement is shown in Figure 20.

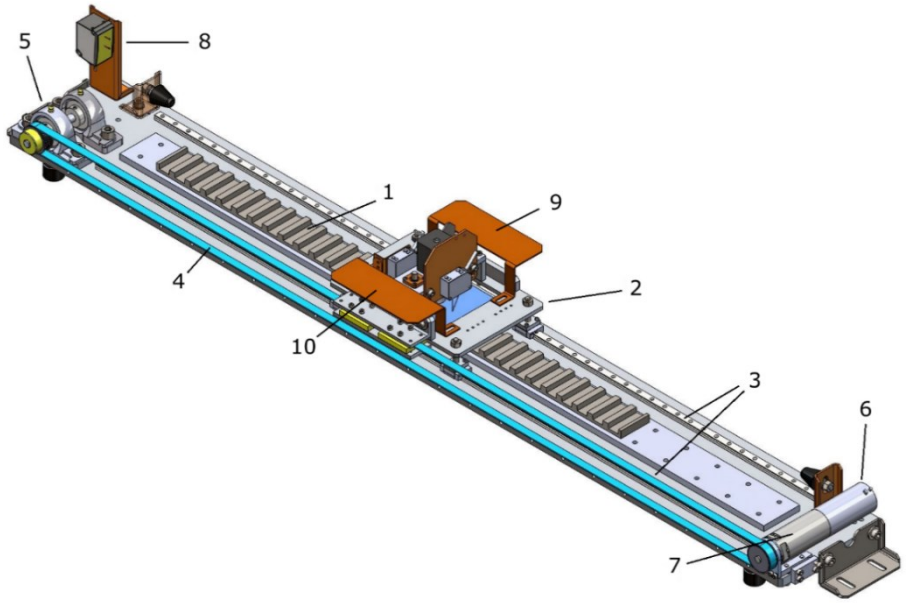

Figure 20: test arrangement comprising a stator rail (1), carrier (2), bearing bars (3), cogged belt (4), sheave (5), servo motor (6), reduction gear (7), third reference laser (8), second support bracket (9) and third support bracket (10).

The carrier comprises a first support bracket where a stepper motor is attached. It is controlled with a separate controller that is attached to a second support bracket on the carrier. The stepper motor has a screw type axis to provide linear motion towards the stator rail. There is an opening in the carrier between the stepper motor and the stator rail. An acrylic plate is attached to the axis of the stepper motor and is bearing-mounted to the first support bracket with two bearings to allow motion only towards the stator rail. Furthermore, the size of the acrylic plate is such that it can move through the opening. Figure 21 shows the structure of carrier in details.

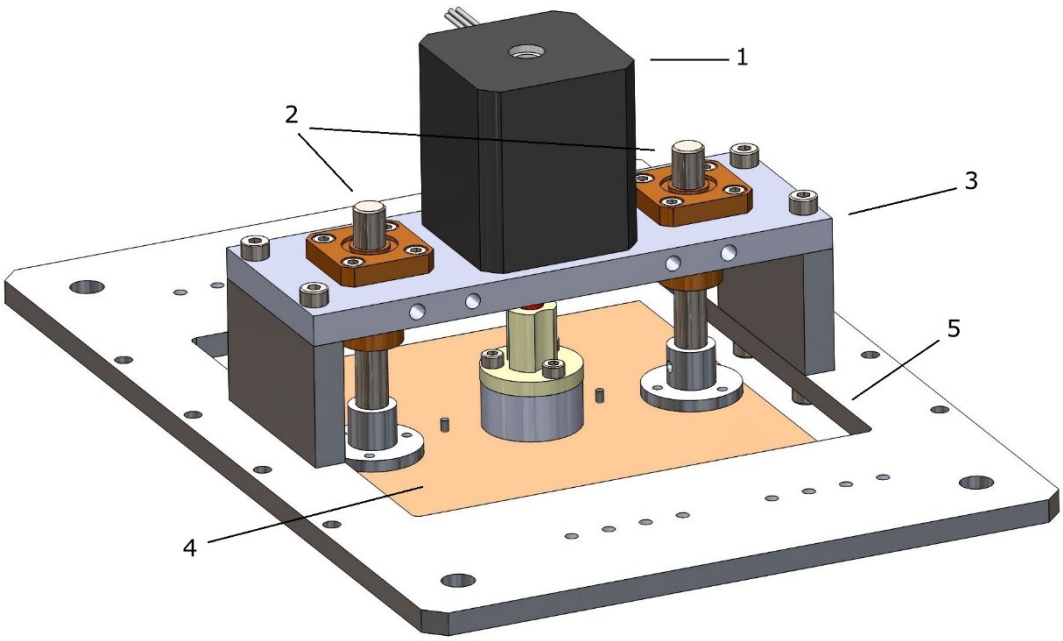

Figure 21: carrier comprising a stepper motor (1), bearings (2), first support bracket (3) and an acrylic plate (4) in an opening (5).

Figure 22 shows how the SPCBs are attached to the bottom of the acrylic plate with screws. The distance to the acrylic plate is 1 cm. Hence, the distance to any possible source of interference on the carrier is increased. The EPCB is attached to the carrier surface on the other side of the acrylic plate. The EPCB and SPCBs are connected with a cable which fits through the opening. Hence, the stepper motor generates the motion of SPCBs towards the stator rail with great repeatability and accuracy. This motion is used to test the air gap sensing of the sensing apparatus prototype.

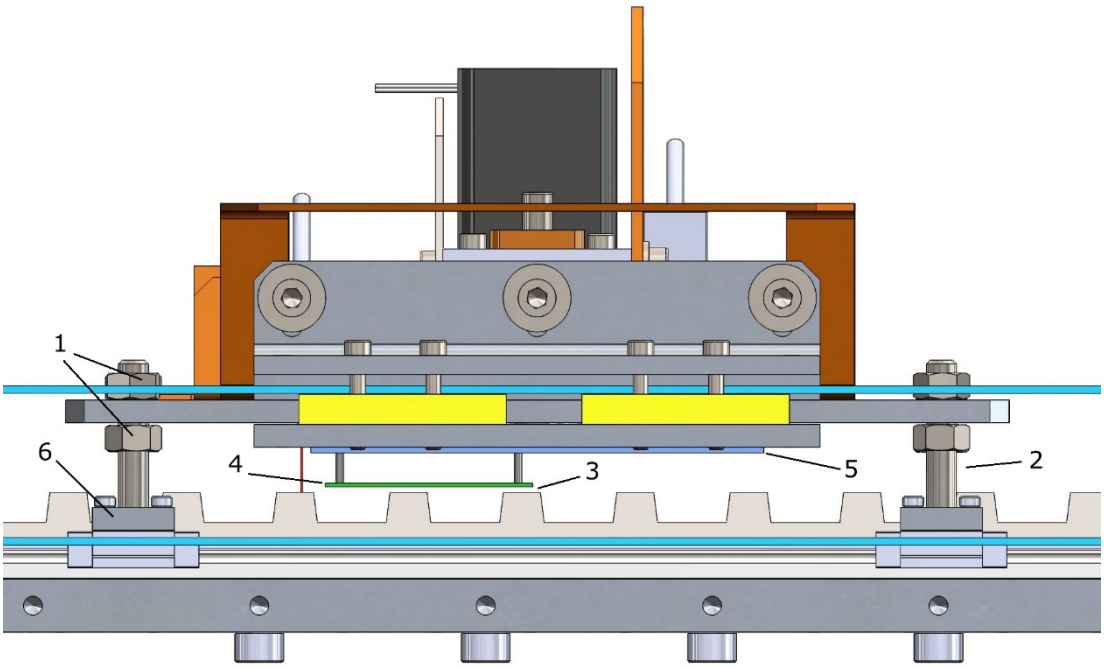

Figure 22: structure of the carrier. It is attached with nuts (1) and screws (2), wherein bearings (6) are attached, above the stator rail forming an air gap (3). Below the carrier, an SPCB (4) is attached to an acrylic plate (5).

First reference laser is attached to the first support bracket above the acrylic plate. It measures the motion of the acrylic plate towards the stator rail and is used as a reference for the air gap sensing results. Second reference laser is attached to the carrier to measure the stator rail profile i.e. teeth under the carrier. It is used as a reference for the rotor position sensing results. The locations of the reference lasers on the carrier are shown in Figure 23.

The motion along the stator rail is generated with a servo motor and a reduction gear which is attached to the axis of the servo motor. A separate controller controls the servo motor which is attached to the end of the framework structure as is shown in Figure 20. The force generating the motion is transferred to the carrier with a cogged belt which is tightened between the servo motor and a sheave on the other side of the framework structure. Hence, the servo motor generates the motion of SPCBs along the stator rail with great repeatability and accuracy. This motion is used to test the rotor position sensing of the sensing apparatus prototype.

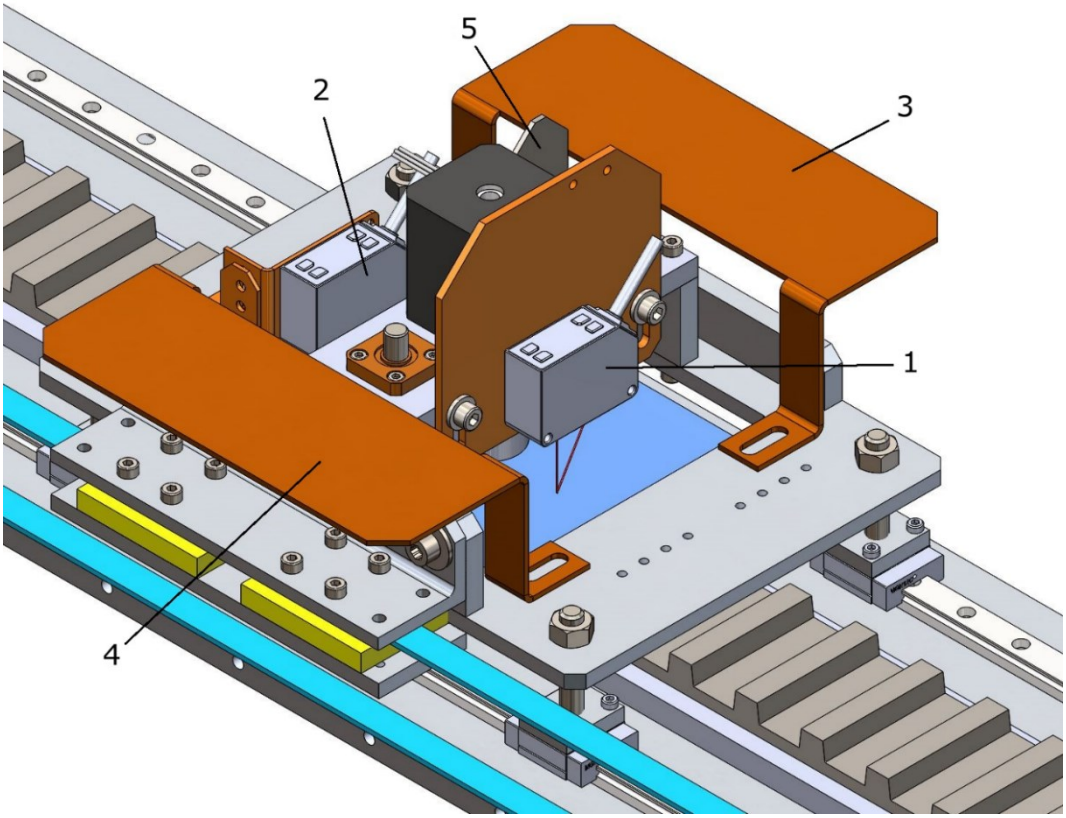

Figure 23: the carrier arrangement where first (1) and second (2) reference lasers, second (3) and third (4) support brackets and a flat counter surface (5) for third reference laser (8) in Figure 20 are attached.

Third reference laser, shown in Figure 20, is attached to the end of the framework structure close to the sheave. It measures the stator rail position of the carrier and is used as a reference for the rotor position sensing results.

A development board comprising a programmable microcontroller is used as a master for the A/D converters on the EPCB. It is attached to the support bracket on the carrier and coupled to a power supply and EPCB input. It is programmed to initialize A/D converters, control their measurement modes, resolution and measurement time t_M and read status and measurement result registers. The programmed master requires $8{,}2$ µs to read a status register and $10{,}3$ µs to read a measurement result.

The master-slave communication and reference laser signals are read with a single logic analyzer. Hence, digital measurement results and analog reference signals are stored

with comparable time stamps and can be further processed and analyzed.

As a summary, a bill of materials for the test arrangement is shown in Table 8, comprising information about manufacturers and product or model names.

Table 8: test arrangement components.

Name	**Manufacturer**	**Product/Model**	**Number in Figures**
Stepper motor	Haydon Kerk	E43M4Y-05-900	1 in Figure 21
Stepper motor controller	Haydon Kerk	PCM4826E-K	
Servo motor	Faulhaber	4490H024BS	6 in Figure 20
Servo motor controller	Faulhaber	MCBL 3006	
Reference laser	SICK	OD Mini	1&2 in Figure 23
Reference laser	SICK	DT35	8 in Figure 20
Logic analyzer	Saleae	Logic Pro 16	

5.2 Tests

Three different tests are performed for the sensing apparatus prototype. The tests are applied for different SPCBs and in every test, a single SPCB is tested at a time. The tests focus to evaluate the resolution, linearity of measurements, average measurement time $\bar{t}_M$ and response times t_{R1} and t_{R2} of the sensing apparatus prototype. Next these evaluated properties are defined and the methods to determine them are described.

The resolution means the smallest distance which the sensing apparatus prototype can measure. It is determined by dividing the measured distance with unique measurement values between that distance. The resolution is calculated from the test measurements and the results are compared with other SPCBs.

The linearity of measurements means the variation of resolution over the tested sensing range. In case of linear measurements, the resolution stays constant over the tested sensing range. This is evaluated by plotting the unique measurement values from the lowest to highest and then visually evaluating the linearity of the plotted curve.

The average measurement time $\bar{t}_M$ is determined by dividing the duration of a test with

the number of measurements during the test. It is calculated from the test measurements and the result is compared with the conversion time t_c of the A/D converter used in that test.

The first response time t_{R1} means the delay between the actual change in the measured system and a response in the output of the sensing apparatus prototype. It is calculated from the test measurements. The second response time t_{R2} is calculated. It is the delay between the actual change in the measured system and the first stable output value of the sensing apparatus prototype. Next each test is briefly described.

The rotor position sensing test

The rotor position sensing test arrangement is such that the air gap between a tested SPCB and the stator rail is fixed, the conversion time t_c is set constant and the carrier is driven with a constant velocity ($0{,}1$ m/s) over two pole pitches. During that, the sensing apparatus prototype measures the frequency of the resonance circuits, the second reference laser measures the stator rail profile and/or the third reference laser measures the carrier position. This test evaluates resolution, linearity of measurements and the average measurement time $\bar{t}_M$ of the sensing apparatus prototype in the rotor position sensing use.

The air gap sensing test

The air gap sensing test arrangement is such that the position of the carrier is fixed, conversion time t_c is set constant and the air gap is changed by first lowering and then rising a tested SPCB above a flat aluminum surface which is used instead of the supporting structure of the stator rail. During that, the sensing apparatus prototype measures the frequency of a resonance circuit and the first reference laser measures the change of air gap. This test evaluates resolution, linearity of measurements and the average measurement time $\bar{t}_M$ of the sensing apparatus prototype in the air gap sensing use.

The response time test

The response time test arrangement is such that the position of the carrier is fixed, conversion time t_c is set constant and the air gap between a tested SPCB and the flat aluminum surface is fixed. Additionally, a solid-state switch is coupled in series with one resonance circuit on the tested SPCB. The circuit diagram of the response time test arrangement is shown in Figure 24. During the response time test, the sensing apparatus prototype measures the frequency of the resonance circuit while the solid-state switch is controlled from a non-conductive state to conduct. The control signal of the solid-state switch and the output of the sensing apparatus prototype are measured. Hence, the SPCB does not move but the change in the state of the solid-state switch is considered as an instant change of the air gap and therefore the response times t_{R1} and t_{R2} are measured from the change of the control signal state. This test evaluates the average measurement time $\bar{t}_M$ and the response times t_{R1} and t_{R2} of the sensing apparatus prototype.

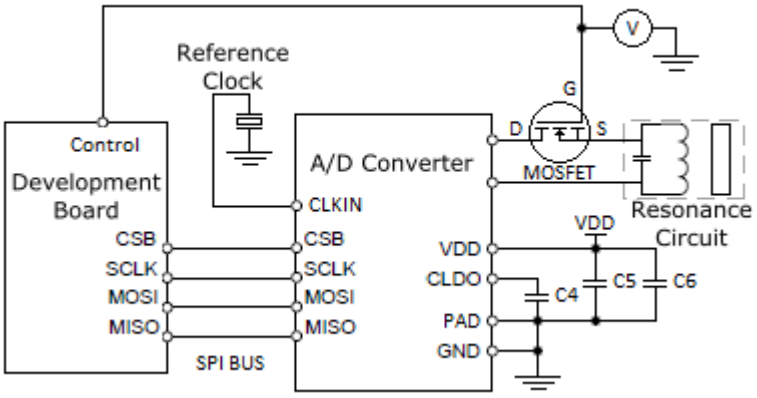

Figure 24: circuit diagram of the response time test arrangement.

5.3 Results

This chapter summarizes results of each test separately. The rotor position sensing test results are presented and discussed first, then the air gap sensing test results and lastly the response time test results.

The rotor position sensing test results

Next, the rotor position sensing tests (tests 1-7) are presented. In all of them, the air gap was set to $1{,}25$ mm. In tests 1 and 3, the SPCB with circular sensing coils and operating frequency close to $3{,}3$ MHz was tested. During test 1, only one resonance circuit was activated and the conversion time t_c of the A/D converter on the EPCB operating the active resonance circuit was set to 100 µs. In test 3, only the conversion time t_c was changed to 40 µs compared to test 1. In tests 2 and 4, the SPCB with octagonal sensing coils and operating frequency close to $1{,}5$ MHz was tested. As in tests 1 and 3, only one resonance circuit was activated. The conversion time t_c was 100 µs in test 2 and 40 µs in test 4. In tests 5 and 7, the SPCB with circular sensing coils and operating frequency close to $1{,}5$ MHz was tested. Conversion time $t_c = 100$ µs was used in both tests. In test 5, two resonance circuits were activated and in test 7, three resonance circuits were activated. In test 6, the SPCB with square sensing coils and operating frequency close to $1{,}5$ MHz was tested with conversion time $t_c = 100$ µs. In that test two resonance circuits were activated.

In test 1, resonance circuit 1 on the SPCB was activated (its location on the SPCB is shown in Figure 15). The measured resonance circuit output signal S_1 is shown in Figure 25 when the SPCB travels over a single pole pitch. An output voltage of the second reference laser, measuring the profile of the stator rail, is used as a reference in test 1. Peaks in the reference laser output signal (before t_1, at $0{,}925$ s and before t_4) are interference which occurs when the reference laser beam reflects from the edges of stator rail teeth. Threshold value T_1 in the figure, is 80 percent of the peak-to-peak amplitude of the resonance circuit output signal S_1. Threshold value T_2 is 20 percent. Same threshold values were used for all rotor position sensing tests. The rising slope of S_1 between the threshold values (from t_2 to t_3) is selected to be used for the calculation of sensing resolution. In test 1, the distance that the SPCB travels between t_2 and t_3 is $3{,}64$ mm.

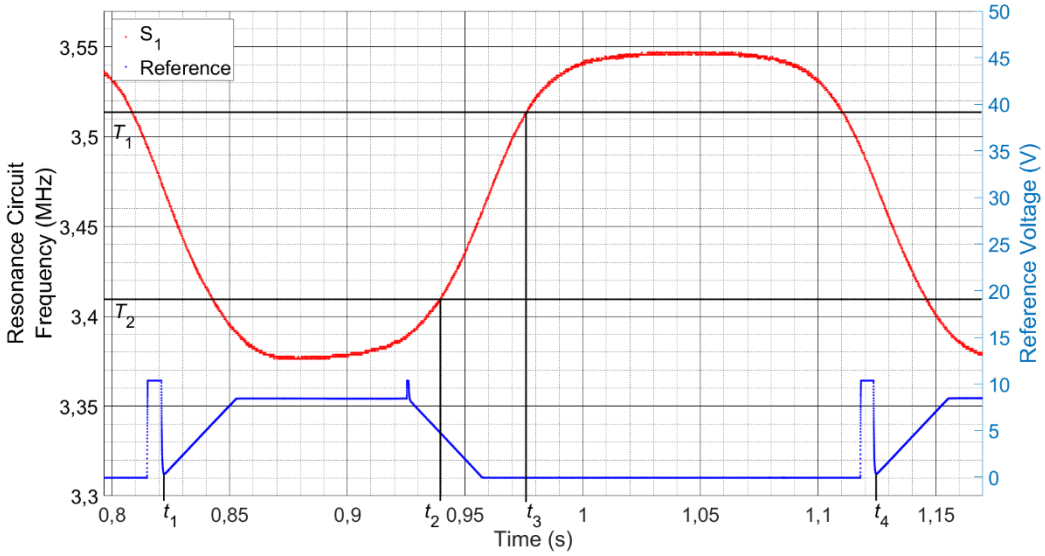

Figure 25: A/D converter output as a function of time while traveling along the stator rail.

Figure 26 shows the linearity of measurements in test 1. There are 134 unique measurement values between T_1 and T_2. Hence, the resolution is calculated by dividing $3{,}64$ mm by 134, resulting $27{,}2$ µm.

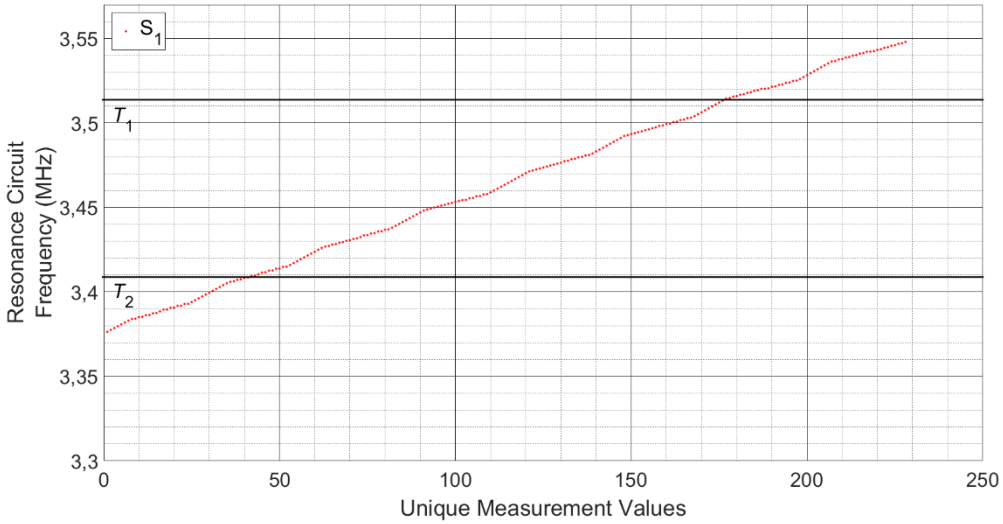

Figure 26: unique A/D converter output values of Figure 25.

In test 1, the calculated average measurement time $\bar{t}_M$ is $99{,}25$ µs. Figure 27 shows how the actual measurement time t_M between single measurement values is varying. This variation is at least partly caused by the development board program and A/D converters not being synchronized and therefore the measurement results are read from the A/D converter registers irregularly.

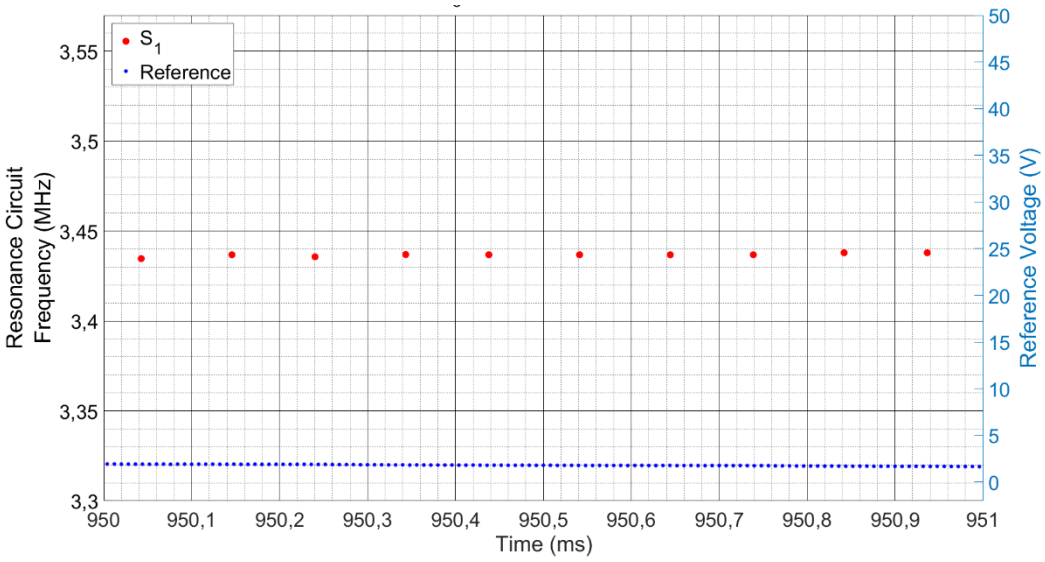

Figure 27: A/D converter output as a function of time while traveling along the stator rail. This is Figure 25 zoomed to show the measurement time.

Figure 28 shows resonance circuit output signals S_1 and S_5 of test 5. On the crossing points of resonance circuit output signals, the signals have interference. This interference is most likely caused by a cross coupling of the resonance circuit output signals in the cable between EPCB and SPCB. The cable was not insulated and in the cable, the signal lines were $0{,}5$ mm apart each other.

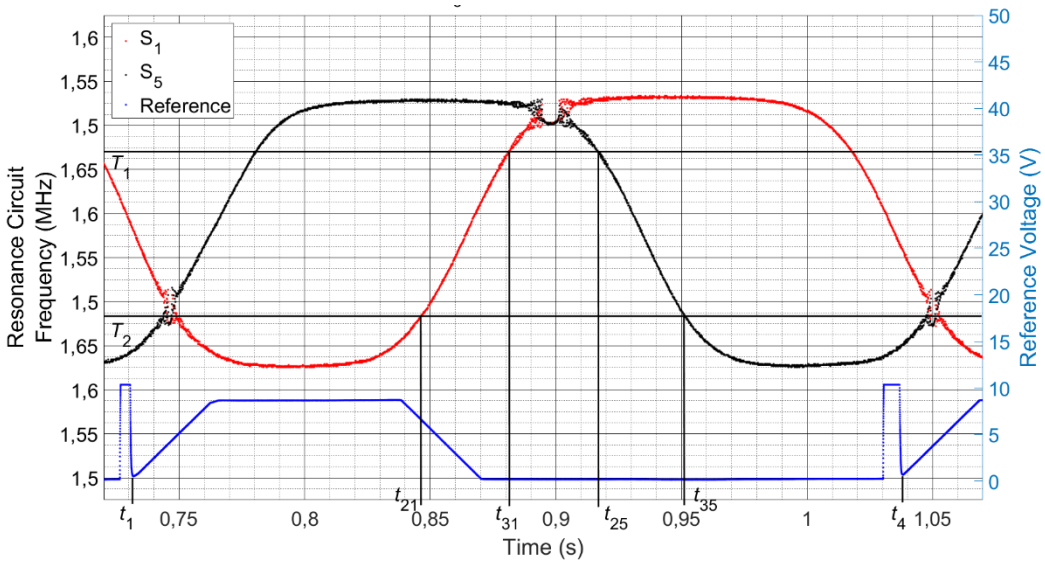

Figure 28: A/D converter outputs as a function of time while traveling along the stator rail.

Figure 29 shows resonance circuit output signals S_1, S_3 and S_5 of test 7. The interferences on the lower crossing points in tests 5 and 7 are between the threshold values T_1 and T_2. Hence, they would affect the position sensing resolution.

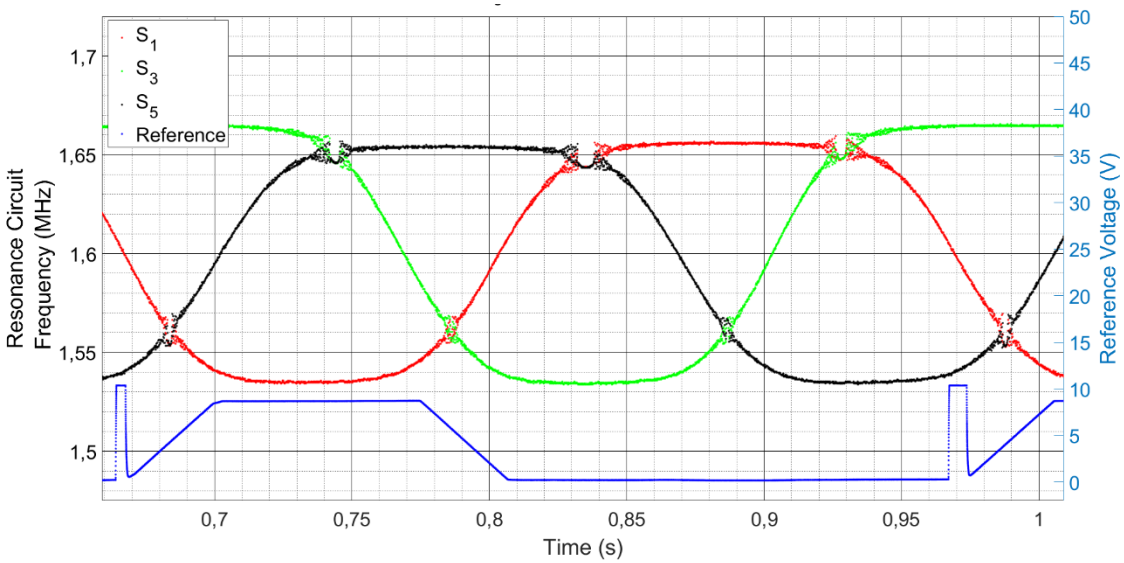

Figure 29: A/D converter outputs as a function of time while traveling along the stator rail.

Figure 30 shows difference signals generated from the resonance circuit output signals of test 7. The difference signals do not have interference on the rising slopes which can be used for rotor position sensing. Also, the peak-to-peak amplitudes of the difference signals are approximately double compared to the signals which they are generated from.

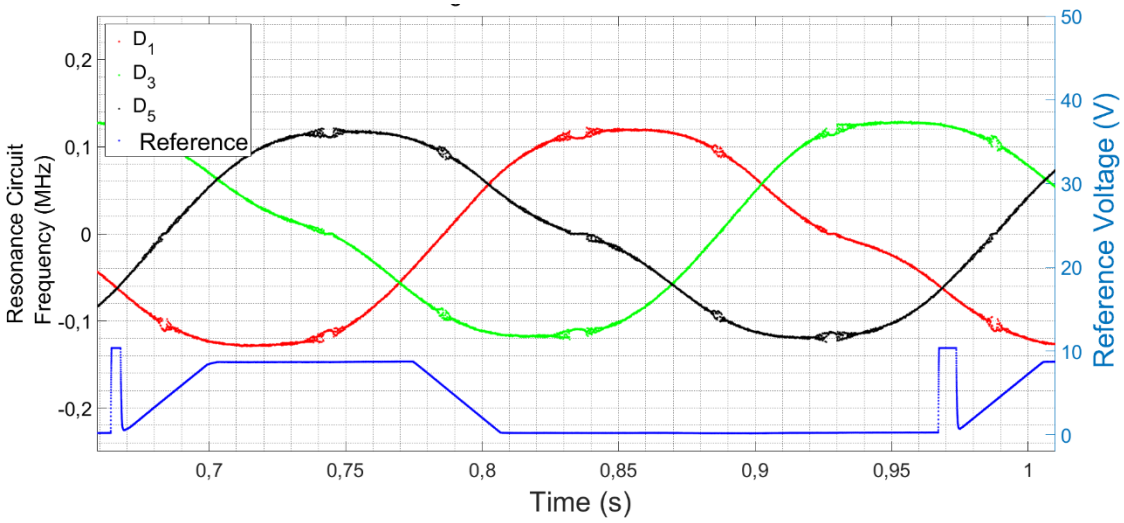

Figure 30: Difference signals generated from A/D converter output signals in Figure 29.

The results of the rotor position sensing tests 1-6 are shown in Table 9. Based on the results, the prototype reached the rotor position sensing requirements set for the resolution and measurement time t_M. More information about the rotor position sensing tests is presented in Appendix A.

Table 9: rotor position sensing test results.

	Test 1	**Test 2**	**Test 3**	**Test 4**	**Test 5**	**Test 6**
Shape of the sensing coil	Circular	Octagonal	Circular	Octagonal	Circular	Square
Conversion time t_c [µs]	100	100	40	40	100	100
Average measurement time $\bar{t}_M$ [µs]	99,3	99,3	39,0	39,0	99,0	99,3
Resolution [µm]	27	19	72	46	13	15

The linearity of measurements was better with SPCBs that had higher inductance and lower operating frequency. The shape of the sensing coils did not appear to have visually noticeable difference on the results. Test 2 results had noticeably better linearity of measurements, shown in Figure 31, compared to the linearity of test 1 results shown in Figure 26. Overall, the linearity of measurements appeared to be sufficient to the rotor position sensing use.

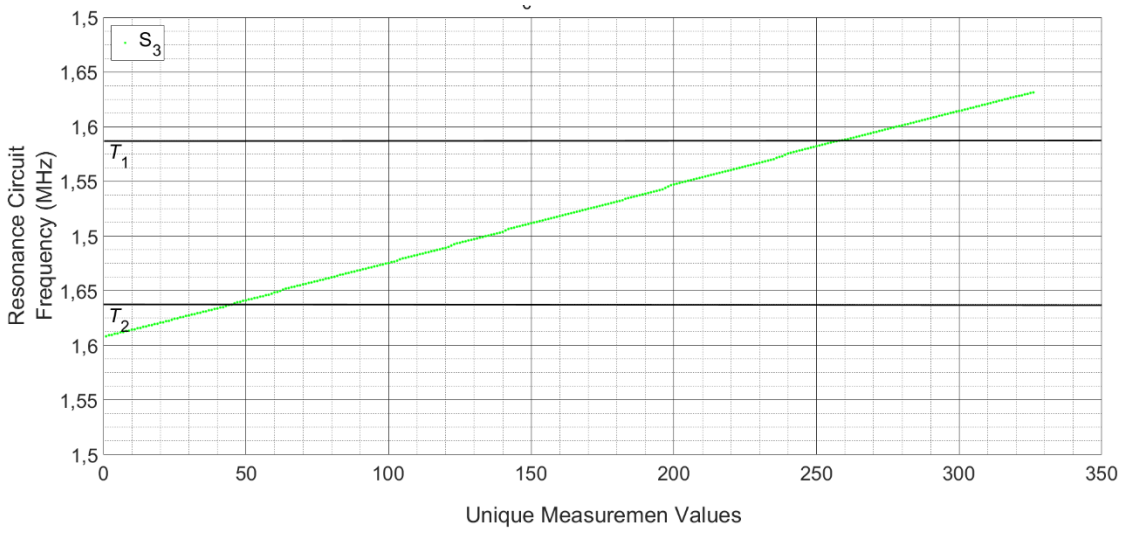

Figure 31: unique A/D converter output values of Figure 37.

The air gap sensing test results

Next, the air gap sensing tests (tests 8 and 9) are presented. In both, the air gap was initially set to $2{,}5$ mm, then changed to 0 mm and finally returned to $2{,}5$ mm. Also, SPCB with octagonal sensing coils and operating frequency close to $1{,}5$ MHz was used for both tests. Furthermore, only one resonance circuit was activated and the same resonance circuit was used for both tests. The conversion time t_c was set to 100 µs in test 8 and 50 µs in test 9.

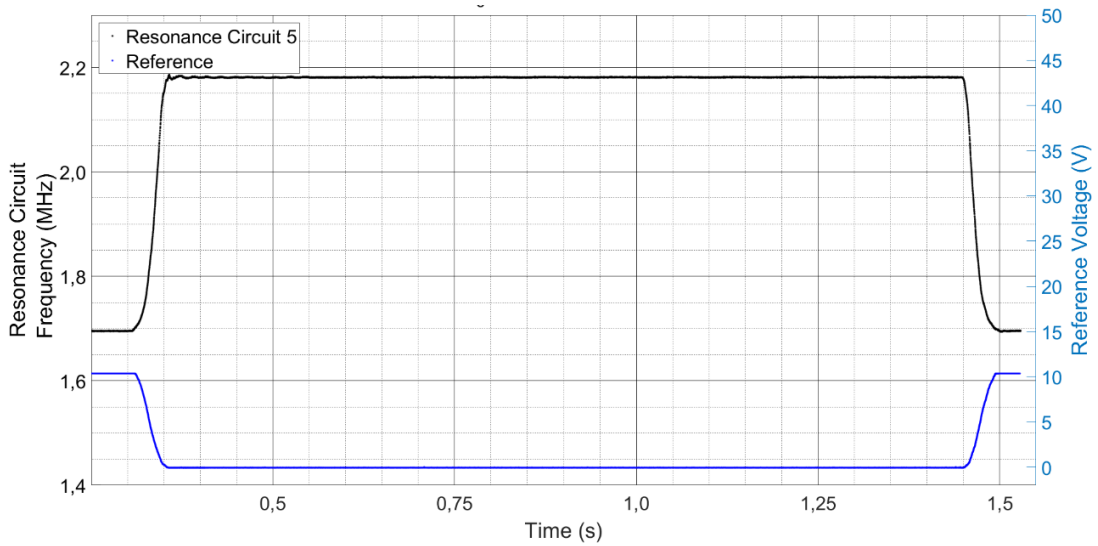

Figure 32: A/D converter output as a function of time during the air gap sensing test.

Figure 32 shows test 8. Contrary to the rotor position tests, the frequency of resonance circuit increased when it got closer to the measured object. As the measurement was done above a flat aluminum surface instead of laminated stator rail, eddy currents were generated, which is seen as an opposite behavior of resonance circuit frequency. An output voltage of the first reference laser is used as a reference in air gap sensing tests.

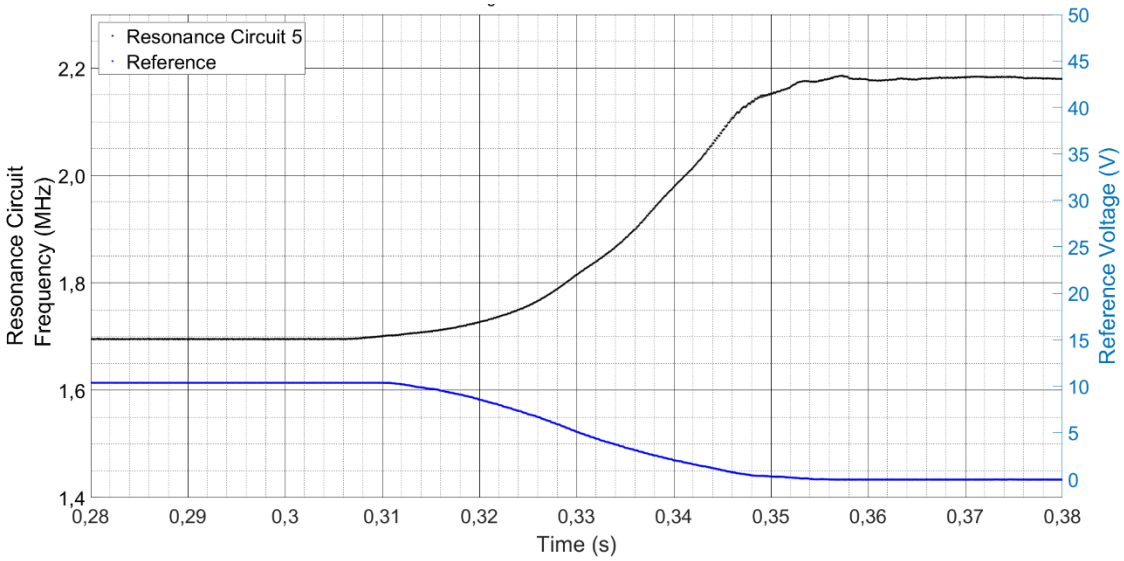

Figure 33: A/D converter output as a function of time while lowering the SPCB. This is Figure 32 zoomed in on the start of lowering.

Figure 33 shows the first change in the air gap of test 8 and Figure 34 shows when the air gap is returned to the initial value. As these figures show, the change in frequency appears to be exponential although the reference signal is linear. However, the response to the change in the air gap can be seen first in the resonance circuit output and then in the reference signal.

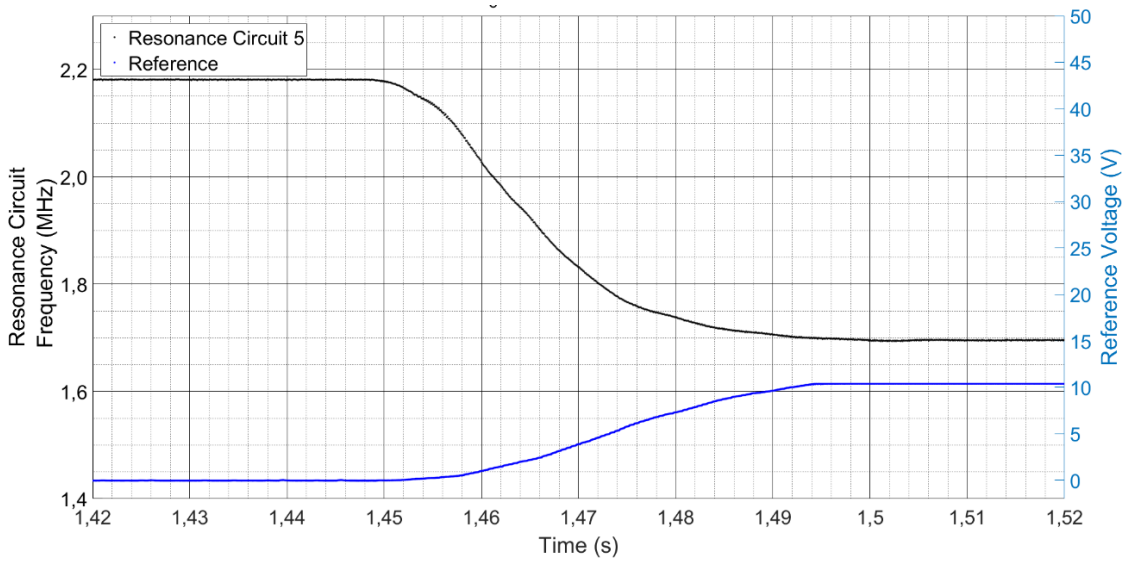

Figure 34: A/D converter output as a function of time while lifting the SPCB. This is Figure 32 zoomed in on the start of lifting.

In air gap sensing tests, the linearity of measurements was noticeably worse than in rotor position sensing tests. Figure 35 shows the linearity of test 8 measurements. The curve appears to have the shape of letter “S” which should be compensated when determining the position.

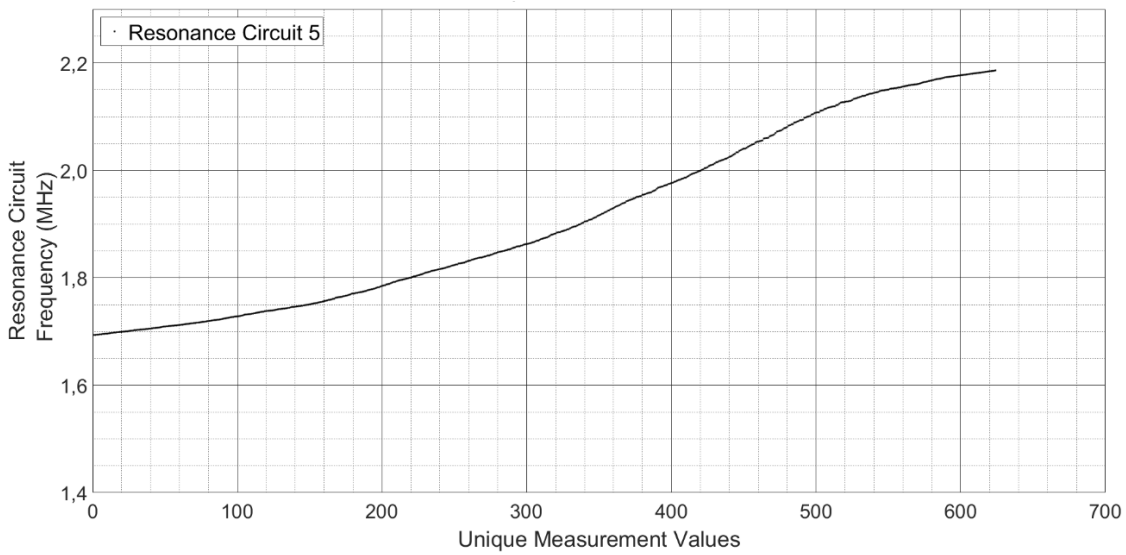

Figure 35: unique A/D converter output values of Figure 32.

The air gap sensing test results are shown in Table 10. Based on the results, the prototype reached the air gap sensing requirements set for the resolution and measurement time. More information about the air gap sensing tests is presented in Appendix B.

Table 10: air gap sensing test results.

	Test 8	**Test 9**
Shape of the sensing coil	Octagonal	Octagonal
Conversion time t_c [µs]	100	50
Average measurement time $\bar{t}_M$ [µs]	99,3	46,6
Resolution [µm]	4,0	4,4

The response time test

Next, the response time tests (tests 10-14) are presented. In all tests, SPCB with hexagonal sensing coils and operating frequency close to 1,5 MHz was tested. Furthermore, only one resonance circuit was activated and the same resonance circuit was used for every test. In test 10, the conversion time t_c was set to 100 µs. In the other tests, 200 µs was used. The air gap was 0 mm in test 11, 1,47 mm in tests 10 and 12, 4,7 mm in test 13 and 7,8 mm in test 14.

Figure 36 shows the frequency of the resonance circuit in test 11. In the figure, the voltage of the control signal of the solid-state switch is used as a reference. The solid-state switch is not conducting before t_2, but the A/D converter measures low frequency. After t_2 first response time $t_{R1} = t_3 - t_2 = 80$ µs and second response time $t_{R2} = t_4 - t_2 = 290$ µs are measured. The measured frequency value at t_3 is approximately an average of frequency values between t_1 and t_3 if before t_2 frequency value is the same as at t_1 and after t_2 the frequency value is the same as at t_4.

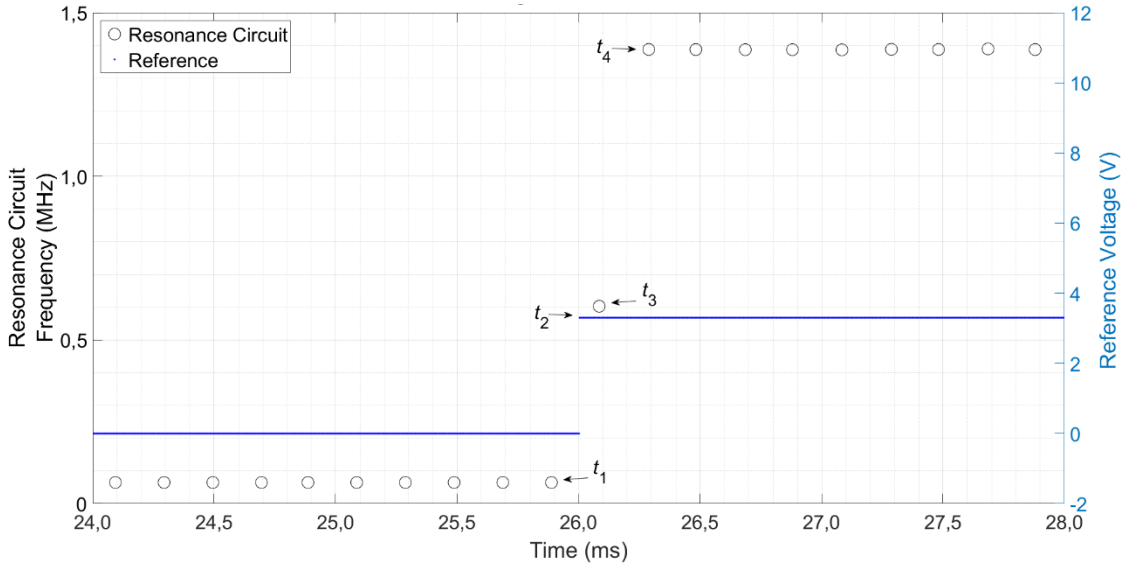

Figure 36: response time test above a flat aluminum surface.

The results of response time tests are shown in Table 11. Based on the results, the first response time t_{R1} is equal to or less than the measurement time t_M and the second response time t_{R2} is between t_M and $2t_M$. More information about the response time tests is in Appendix C.

Table 11: response time test results.

	Test 10	**Test 11**	**Test 12**	**Test 13**	**Test 14**
Shape of the sensing coil	Hexagonal	Hexagonal	Hexagonal	Hexagonal	Hexagonal
Conversion time t_c [µs]	100	200	200	200	200
Average measurement time $\bar{t}_M$ [µs]	99,2	199,3	199,4	199,3	199,4
Air gap [mm]	1,47	0	1,47	4,8	7,8
Response time t_{R1} [µs]	40	80	100	90	100
Response time t_{R2} [µs]	140	290	300	290	310

6 Summary

The main objective of this thesis was to develop a sensing apparatus or a solution which could measure the air gap and position of a mover in a linear motor application within the measurement time and accuracy requirements. An inductive rotor position sensor used in a similar linear motor application was studied and further developed. Based on that, a sensing apparatus prototype was designed and manufactured. Also, a test arrangement was designed and built. Finally, the sensing apparatus prototype was tested with the test arrangement.

Based on test results, the sensing apparatus prototype fulfilled the requirements which were set for the rotor position and air gap sensing. Also, the generated difference signals appeared to correspond to the sine wave approximated difference signals. Hence, the presented look-up table method appears to be feasible for the rotor position sensing. However, as the accuracy of rotor position sensing was tested with a constant air gap, further development is needed for the rotor position sensing with a varying air gap. Also, the air gap sensing was tested only above a flat aluminum surface. Therefore, further study should be done to verify reliable air gap sensing from the supporting structure of the stator rail.

All things considered, the inductive air gap and rotor position sensing appeared to be promising and suitable for this application. The requirements were met and hence this thesis achieved its objective.

7 References

Guaraglia, D. O., & Pousa, J. L. (2014). *Introduction to modern instrumentation - for hydraulics and environmental sciences* De Gruyter.978-3-11-040171-4

Ida, N., Dudley K. (2013). Inductive sensors. In K. Dudley (Ed.), *Sensors, actuators, and their interfaces: A multidisciplinary introduction.* Institution of Engineering and Technology. 793 p. ISBN 978-1-5231-0529-8

Ning, H., Song, X., Zhiqiang, L., & Jingnan, Z. (2012). *Analysis and optimal design of relative position detection sensor for high speed maglev train*. Paper presented at the 2012 Fifth International Conference on Intelligent Computation Technology and Automation, Zhangjiajie, Hunan, China. 89-93 p. ISBN 978-1-4673-0470-2. doi:10.1109/ICICTA.2012.29

Ning, H., Zhiqiang, L., Song, X., & Fengshan, D. (2013). *Optimal design of detection coil of relative position detection sensor for high speed maglev train*. Przegląd Elektrotechniczny, 89(1b). 29-32 p. ISSN 0033-2097

Pippuri, J. (2010). *Finite element analysis of eddy Current Losses in steel laminations of inverter-fed Electrical machines*. Doctoral dissertation. Espoo, Finland: Aalto University, Department of Electrical Engineering. 136 p. ISSN 1795-4584

Song, X., Chunhui, D., & Zhiqiang, L. (2010). *Research on location and speed detection for high speed maglev train based on long stator*. Paper presented at the 2010 8th World Congress on Intelligent Control and Automation, Jinan, China. 6953-6958 p. ISBN 978-1-4244-6712-9. doi:10.1109/WCICA.2010.5554259

Song, X., Ning, H., & Zhiqiang, L. (2012b). *Electromagnetic field analysis and modeling of a relative position detection sensor for high speed maglev trains*. Sensors, 12(5). 6447-6462 p. ISSN 1424-8220. doi:10.3390/s120506447

Song, X., Zhiqiang, L., Ning, H., & Wensen, C. (2012a). *A high precision position sensor design and its signal processing algorithm for a maglev train*. Sensors, 12(5). 5225-5245 p. ISSN 1424-8220. doi:10.3390/s120505225

Steimel, A. (2008). *Electric traction-motive power and energy supply: Basics and practical experience*. 2nd edition. Mercury Learning and Information. 416 p. ISBN 978-1-5231-0016-3

Suhas, R. C., & Oberhauser, C. A. (2016). Motor speed and position sensing using inductive sensing (LDC) technology. *2016 IEEE Annual India Conference (INDICON),* 1-6. doi:10.1109/INDICON.2016.7839101

Texas Instruments. (2015). *LDC1101 1.8-V high-resolution, high-speed inductance-to-digital converter.* Online datasheet. Rev. D. Cited 31.3.2017. Available at: http://www.ti.com/product/LDC1101/technicaldocuments

US 005434504 A. (1995). *Position sensors for linear motors including plural symmetrical fluxes generated by a planar drive coil and received by planar sense coils being colinear along an axis of motion*. International Business Machines Corporation, Armonk, N.Y. US. (Hollis, R. L., Ish-Shalom, J., & Yarmchuk, E. J.) US130228. 1.10.1993. Publ. 18.7.1995. 18 p.

US 20130200884 A1. (2013). *Position sensor*. Aisan Kogyo Kabushiki Kaisha, Obu-shi, JP. (Yuichi, M., & Tetsuji, I.) US13754332. 30.1.2013. Publ. 8.8.2013.

Wang, M. (2005). *Understandable electric circuits*. London, United Kingdom: Institution of Engineering and Technology. 378 p. ISBN 978-0-86341-952-2

Wilson, J. S. (2004). *Sensor technology handbook*. Elsevier. 691 p. ISBN 978-0-7506-7729-5

WO 03002948 A1. (2003). *A method, device and system to determine gear tooth position*. ABB Group Services Center Ab, Västerås, SE. (Eidenvall, A., & Linder, S.) PCT/SE02/01253. 26.6.2002. Publ. 9.1.2003. 29 p.

WO 2013032525 A1. (2013). *A system and method for position sensing*. Persimon Technologies Corporation, Wakefield, US. (Hosek, M.) PCT/US2012/000376. 31.8.2012. Publ. 07.03.2013.

WO 2016206757 A1. (2016). *Elevator with linear motor*. Kone Corporation, Helsinki, FI. (Purosto, T., Hakala, T., Ratia, J., & Petrov, I.) PCT/EP2015/064535. 26.6.2015. Publ. 29.12.2016. 37 p.

Zuk, S., Pietrikova, A., & Vehec, I. (2016). *Development of planar inductive sensor for proximity sensing based on LTCC*. Paper presented at the 2016 39th International Spring Seminar on Electronics Technology (ISSE), Pilsen, Czech Republic. 413-417 p. ISBN 978-1-5090-1389-0. doi:10.1109/ISSE.2016.7563231

8 Appendix

A Rotor Position Sensing Results

Following values are calculated from rotor position sensing tests:

Threshold limit 1 is calculated with

$$T_1 = 0{,}8\ \hat{S}_i \tag{13}$$

where $\hat{S}_i$ is peak-to-peak amplitude of resonance circuit output signal.

Threshold limit 2:

$$T_2 = 0{,}2\ \hat{S}_i \tag{14}$$

Mover (carrier) velocity

$$v_m = \frac{l_{PP}}{t_4 - t_1} \tag{15}$$

where t_1 and t_4 are the time.

The distance the carrier travels during the rising slope between T_2 and T_1:

$$\Delta l_{32} = v_m(t_{3i} - t_{2i}) \tag{16}$$

where Δl_{32} is distance between t_{2i} and t_{3i}.

The resolution of the sensing apparatus:

$$R\text{esolution} = \frac{\Delta l_{32}}{X_{UV}} \tag{17}$$

where X_{UV} is the number of unique measurement values between T_1 and T_2.

Test 1

Table 12: specifications of SPCB in test 1.

Shape of sensing coils	Circular
Number of sensing coils	1
Air gap [mm]	1,25
Conversion time t_c [µs]	100
Number of sensing coil turns	8
Inductance L [µH]	5,699
Quality factor	45,80
Capacitance [pF]	390

Table 13: measurements of test 1.

	A/D converter 1
Max A/D converter output	$3{,}548 \cdot 10^6$
Min A/D converter output	$3{,}376 \cdot 10^6$
T_1	$3{,}513 \cdot 10^6$
T_2	$3{,}410 \cdot 10^6$
Unique measurement values	228
Unique measurement values between T_1 and T_2	134
t_1 [s]	0,8224
t_2 [s]	0,9396
t_3 [s]	0,9763
t_4 [s]	1,125
Carrier velocity v_m [mm/s]	99,1
Distance between t_{2i} and t_{3i} [mm]	3,64
Measurements between t_{2i} and t_{3i}	367
Resolution [µm]	27,2
Average measurement time $\bar{t}_M$ [µs]	99,2540

Test 2

Table 14: specifications of SPCB in test 2.

Shape of sensing coils	Octagonal
Number of sensing coils	1
Air gap [mm]	1,25
Conversion time t_c [µs]	100
Number of sensing coil turns	11
Inductance L [µH]	11,77
Quality factor	26,37
Capacitance [pF]	1000

Table 15: measurements of test 2.

	A/D converter 3
Max A/D converter output	$1{,}632 \cdot 10^6$
Min A/D converter output	$1{,}543 \cdot 10^6$
T_1	$1{,}614 \cdot 10^6$
T_2	$1{,}561 \cdot 10^6$
Unique measurement values	326
Unique measurement values between T_1 and T_2	196
t_1 [s]	0,7358
t_2 [s]	0,8596
t_3 [s]	0,8964
t_4 [s]	1,039
Carrier velocity v_m [mm/s]	98,9
Distance between t_{2i} and t_{3i} [mm]	3,64
Measurements between t_{2i} and t_{3i}	368
Resolution [µm]	18,6
Average measurement time $\bar{t}_M$ [µs]	99,2541

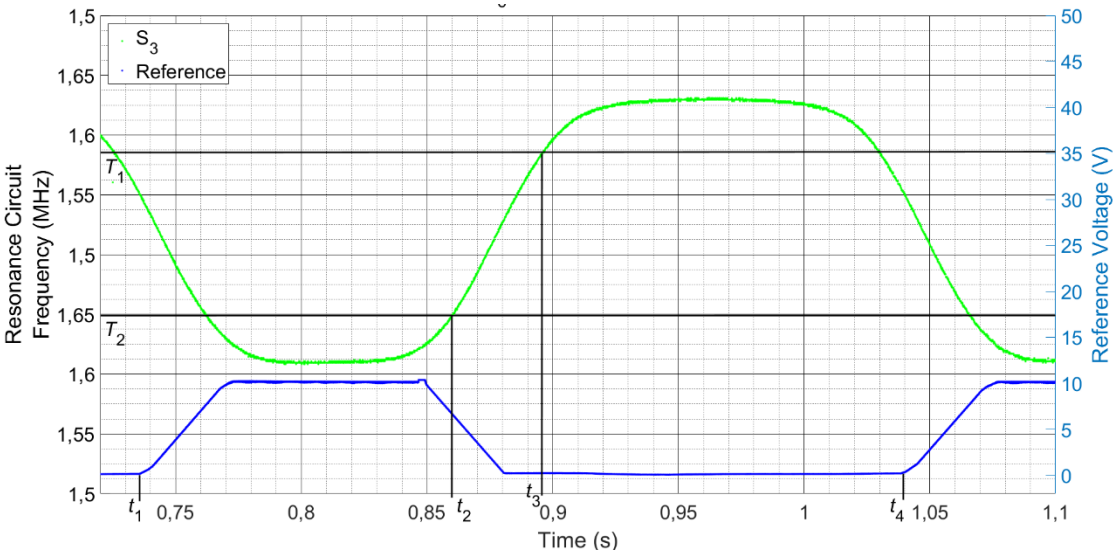

Figure 37: A/D converter output as a function of time while traveling along the stator rail.

Test 3

Table 16: specifications of SPCB in test 3.

Shape of sensing coils	Circular
Number of sensing coils	1
Air gap [mm]	1,25
Conversion time t_c [µs]	40
Number of sensing coil turns	8
Inductance L [µH]	5,699
Quality factor	45,80
Capacitance [pF]	390

Table 17: measurements of test 3.

	A/D converter 1
Max A/D converter output	$3{,}548 \cdot 10^6$
Min A/D converter output	$3{,}373 \cdot 10^6$
T_1	$3{,}513 \cdot 10^6$
T_2	$3{,}408 \cdot 10^6$
Unique measurement values	89
Unique measurement values between T_1 and T_2	55
t_1 [s]	0,6613
t_2 [s]	0,777
t_3 [s]	0,8171
t_4 [s]	0,9644
Carrier velocity v_m [mm/s]	99,0
Distance between t_{2i} and t_{3i} [mm]	3,97
Measurements between t_{2i} and t_{3i}	1002,5
Resolution [µm]	72,2
Average measurement time $\bar{t}_M$ [µs]	38,9658

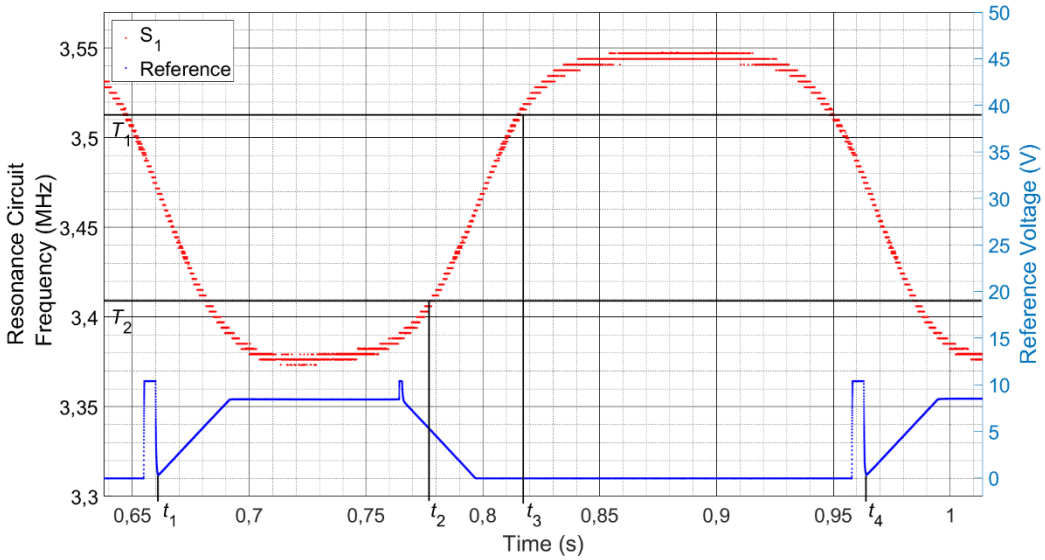

Figure 38: A/D converter output as a function of time while traveling along the stator rail.

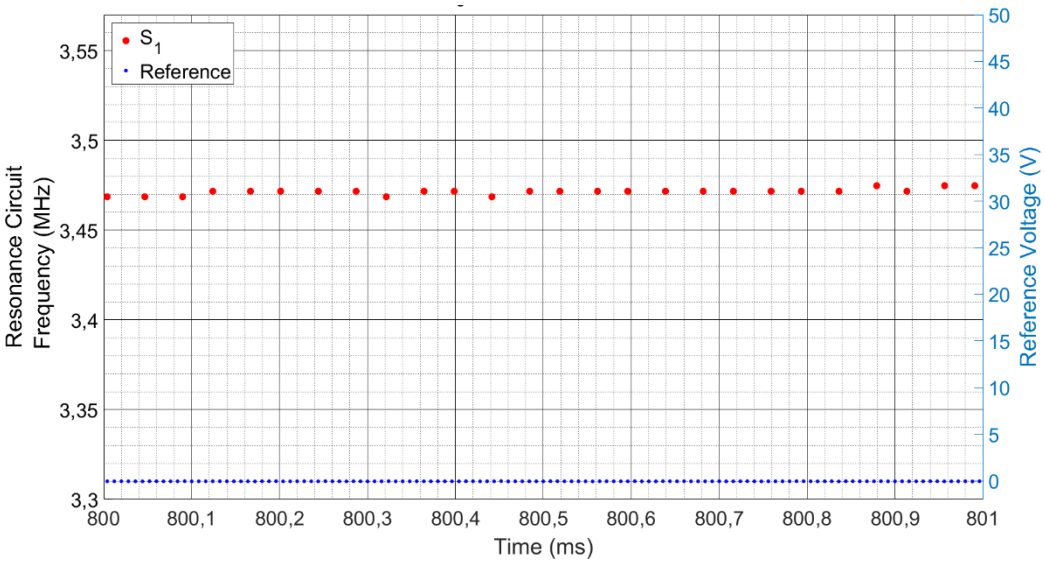

Figure 39: A/D converter output as a function of time while traveling along the stator rail. This is Figure 38 zoomed to show the measurement time.

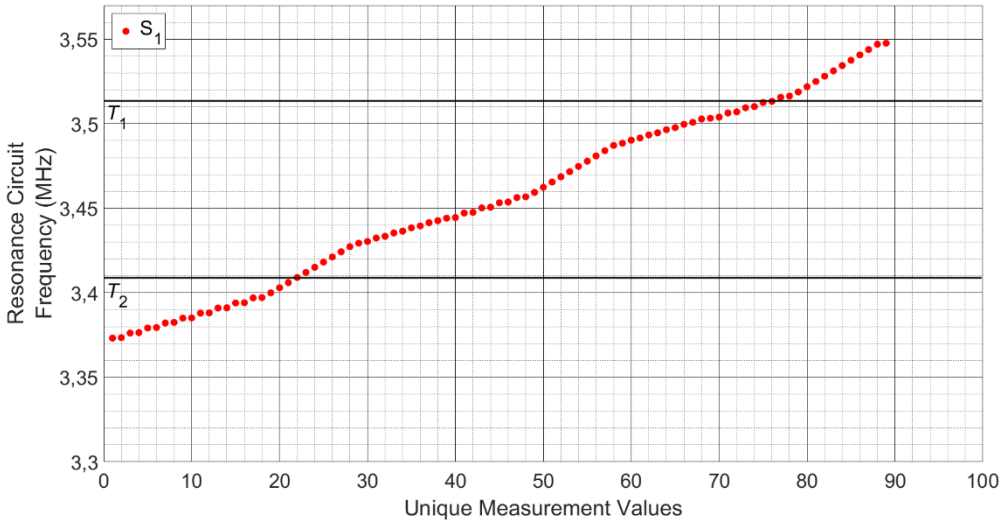

Figure 40: unique A/D converter output values of Figure 38.

Test 4

Table 18: specifications of SPCB in test 4.

Shape of sensing coils	Octagonal
Number of sensing coils	1
Air gap [mm]	1,25
Conversion time t_c [µs]	40
Number of sensing coil turns	11
Inductance L [µH]	11,77
Quality factor	26,37
Capacitance [pF]	1000

Table 19: measurements of test 4.

	A/D converter 3
Max A/D converter output	$1{,}633 \cdot 10^6$
Min A/D converter output	$1{,}543 \cdot 10^6$
T_1	$1{,}615 \cdot 10^6$
T_2	$1{,}561 \cdot 10^6$
Unique measurement values	130
Unique measurement values between T_1 and T_2	79
t_1 [s]	0,9441
t_2 [s]	1,072
t_3 [s]	1,109
t_4 [s]	1,247
Carrier velocity v_m [mm/s]	99,0
Distance between t_{2i} and t_{3i} [mm]	3,66
Measurements between t_{2i} and t_{3i}	925
Resolution [µm]	46,4
Average measurement time $\bar{t}_M$ [µs]	38,9660

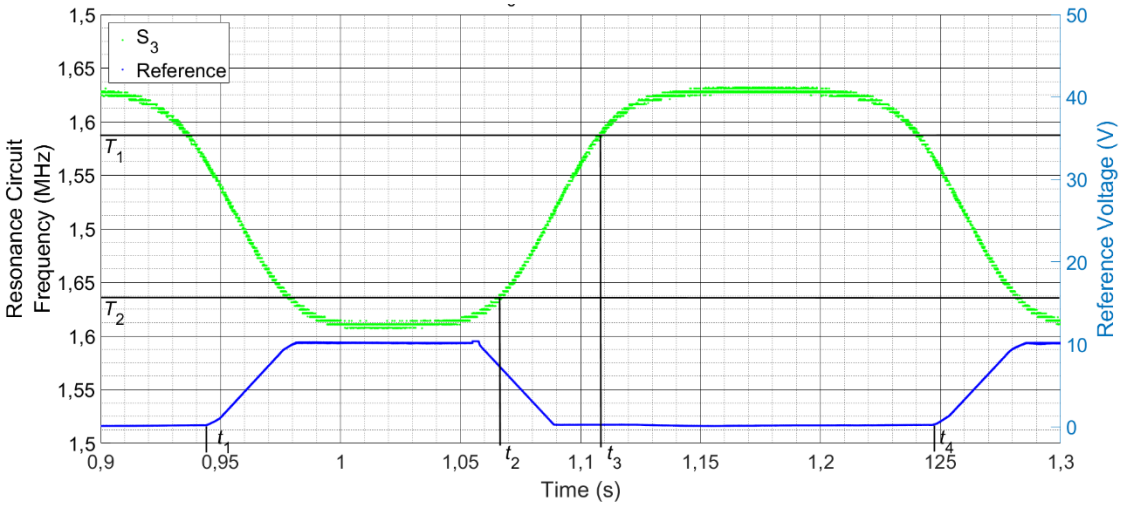

Figure 41: A/D converter output as a function of time while traveling along the stator rail.

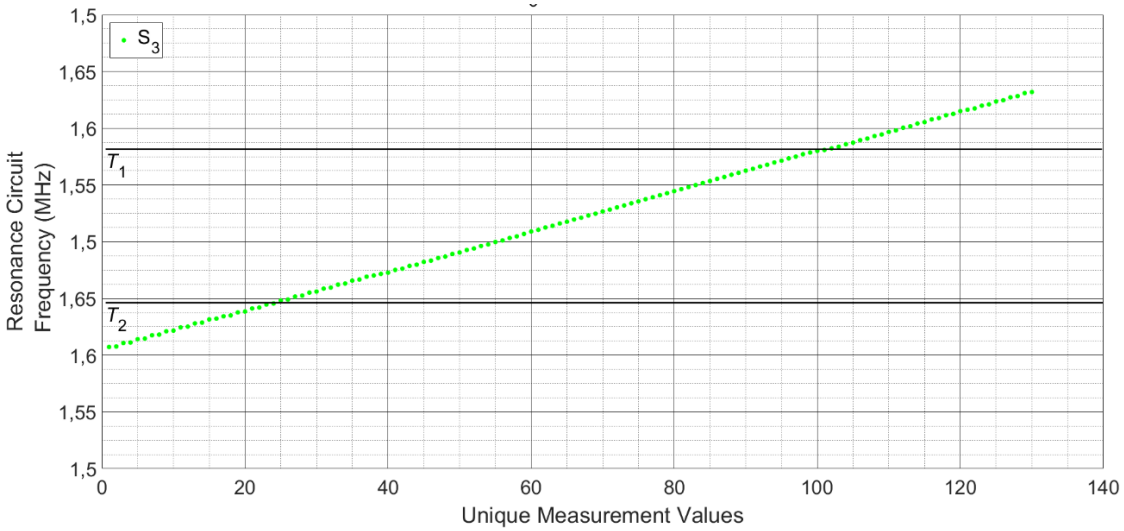

Figure 42: unique A/D converter output values of Figure 41.

Test 5

Table 20: specifications of SPCB in test 5.

Shape of sensing coils	Circular
Number of sensing coils	2
Air gap [mm]	1,25
Conversion time t_c [µs]	100
Number of sensing coil turns	11
Inductance L [µH]	11,52
Quality factor	26,04
Capacitance [pF]	1000

Table 21: measurements of test 5.

	A/D converter 1	**A/D converter 5**
Max A/D converter output	$1{,}653 \cdot 10^6$	$1{,}653 \cdot 10^6$
Min A/D converter output	$1{,}530 \cdot 10^6$	$1{,}530 \cdot 10^6$
T_1	$1{,}628 \cdot 10^6$	$1{,}627 \cdot 10^6$
T_2	$1{,}554 \cdot 10^6$	$1{,}554 \cdot 10^6$
Unique measurement values	444	427
Unique measurement values between T_1 and T_2	262	249
t_1 [s]	0,7319	0,7319
t_{2i} [s]	0,8465	0,9172
t_{3i} [s]	0,8816	0,9513
t_4 [s]	1,038	1,038
Carrier velocity v_m [mm/s]	98,0	98,0
Distance between t_{2i} and t_{3i} [mm]	3,44	3,34
Measurements between t_{2i} and t_{3i}	351	341
Resolution [µm]	13,1	13,4
Average measurement time $\bar{t}_M$ [µs]	98,9866	98,9865

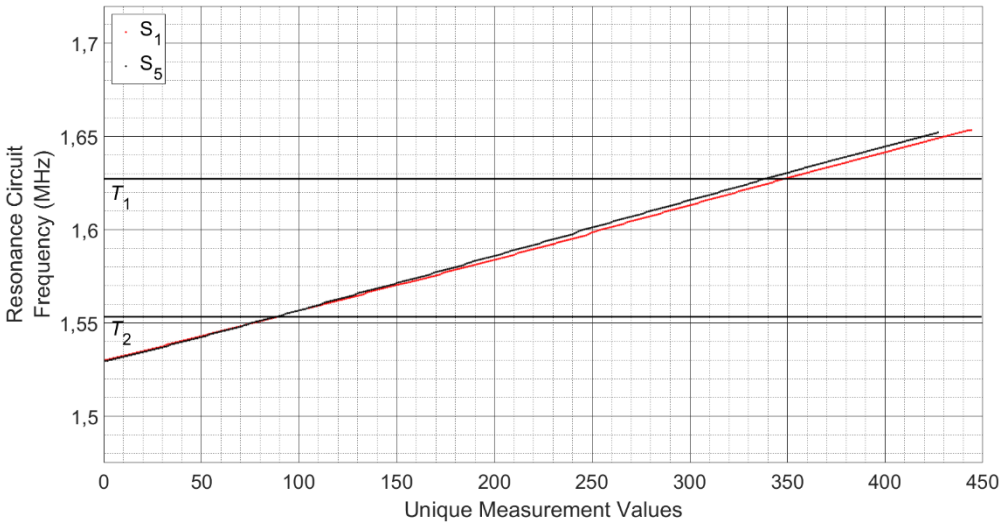

Figure 43: unique A/D converter output values of Figure 28.

Test 6

Table 22: specifications of SPCB in test 6.

Shape of sensing coils	Square
Number of sensing coils	2
Air gap [mm]	1,25
Conversion time t_c [µs]	100
Number of sensing coil turns	11
Inductance L [µH]	13,74
Quality factor	31,35
Capacitance [pF]	820

Table 23: measurements of test 6.

	A/D converter 2	**A/D converter 5**
Max A/D converter output	$1{,}569 \cdot 10^6$	$1{,}569 \cdot 10^6$
Min A/D converter output	$1{,}452 \cdot 10^6$	$1{,}452 \cdot 10^6$
T_1	$1{,}543 \cdot 10^6$	$1{,}546 \cdot 10^6$
T_2	$1{,}479 \cdot 10^6$	$1{,}475 \cdot 10^6$
Unique measurement values	404	433
Unique measurement values between T_1 and T_2	238	252
t_1 [s]	0,6451	0,6451
t_{2i} [s]	0,7940	0,9557
t_{3i} [s]	0,8321	0,9931
t_4 [s]	1,200	1,200
Carrier velocity v_m [mm/s]	99	99
Distance between t_{2i} and t_{3i} [mm]	3,77	3,70
Measurements between t_{2i} and t_{3i}	381	374
Resolution [µm]	15,0	14,7
Average measurement time $\bar{t}_M$ [µs]	99,3482	99,3482

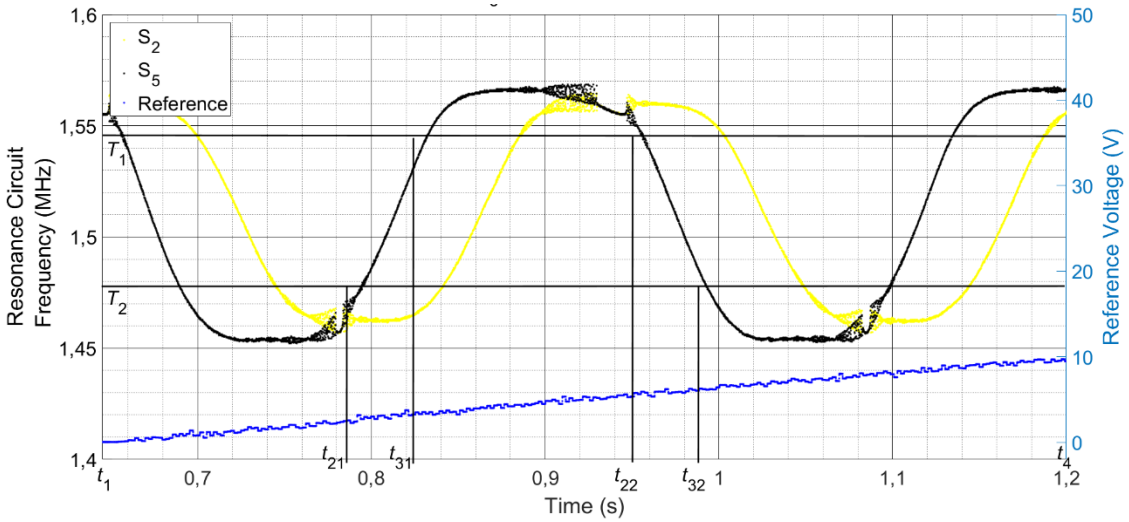

Figure 44: A/D converter outputs as a function of time while traveling along the stator rail.

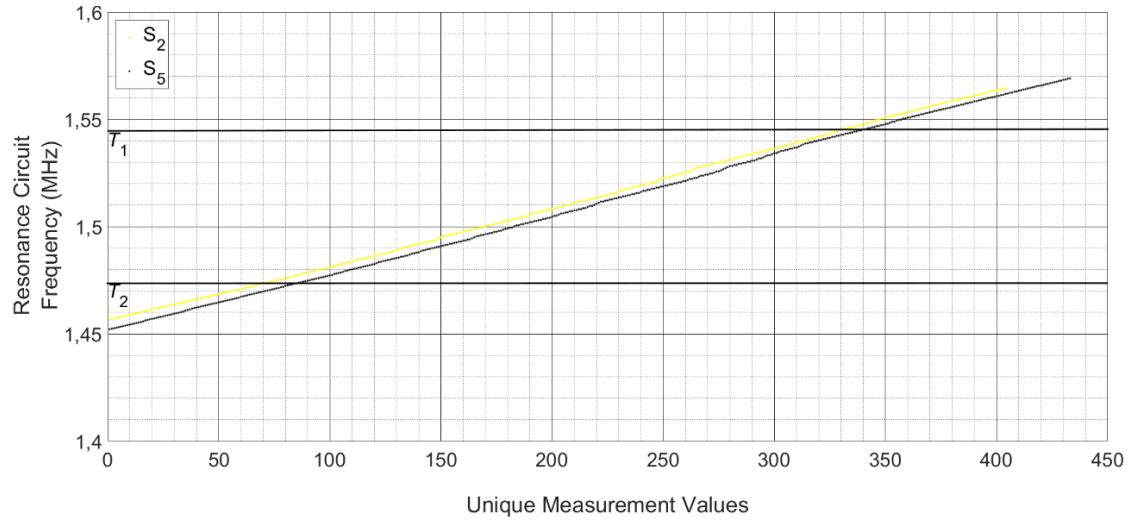

Figure 45: unique A/D converter output values of Figure 44

Test 7

Table 24: specifications of SPCB in test 7.

Shape of sensing coils	Circular
Number of sensing coils	3
Air gap [mm]	1,25
Conversion time t_c [µs]	100
Number of sensing coil turns	11
Inductance L [µH]	11,52
Quality factor	26,04
Capacitance [pF]	1000

Table 25: measurements of test 7.

	A/D converter 1	**A/D converter 3**	**A/D converter 5**
$\bar{t}_M$ [µs]	98,4973	98,4973	98,4973

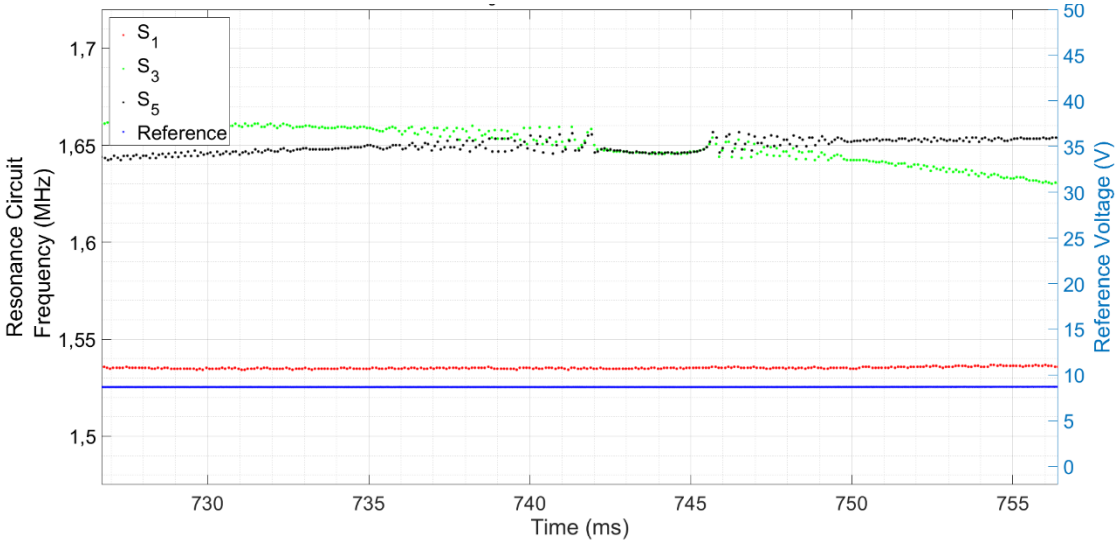

Figure 46: A/D converter outputs as a function of time while traveling along the stator rail zoomed in on the interference.

B Air Gap Sensing Results

Following value is calculated from air gap sensing tests:

Resolution:

$$\text{Resolution} = \frac{[\text{air gap max}] - [\text{air gap min}]}{[\text{unique measurement values}]} \quad (18)$$

Test 8

Table 26: specifications of SPCB in test 8.

Shape of sensing coils	Octagonal
Number of sensing coils	1
Air gap max [mm]	2,5
Air gap min [mm]	0,0
Conversion time t_c [µs]	100
Number of sensing coil turns	11
Inductance L [µH]	11,77
Quality factor	26,37
Capacitance [pF]	1000

Table 27: measurements of test 8.

Unique values	624
Resolution [µm]	4,01
Average measurement time $\bar{t}_M$ [µs]	99,3

Test 9

Table 28: specifications of SPCB in test 8.

Shape of sensing coils	Octagonal
Number of sensing coils	1
Air gap max [mm]	2,5
Air gap min [mm]	0,0
Conversion time t_c [µs]	50
Number of sensing coil turns	11
Inductance L [µH]	11,77
Quality factor	26,37
Capacitance [pF]	1000

Table 29: measurements of test 8.

Unique values	563
Resolution [µm]	4,44
Average measurement time $\bar{t}_M$ [µs]	46,6

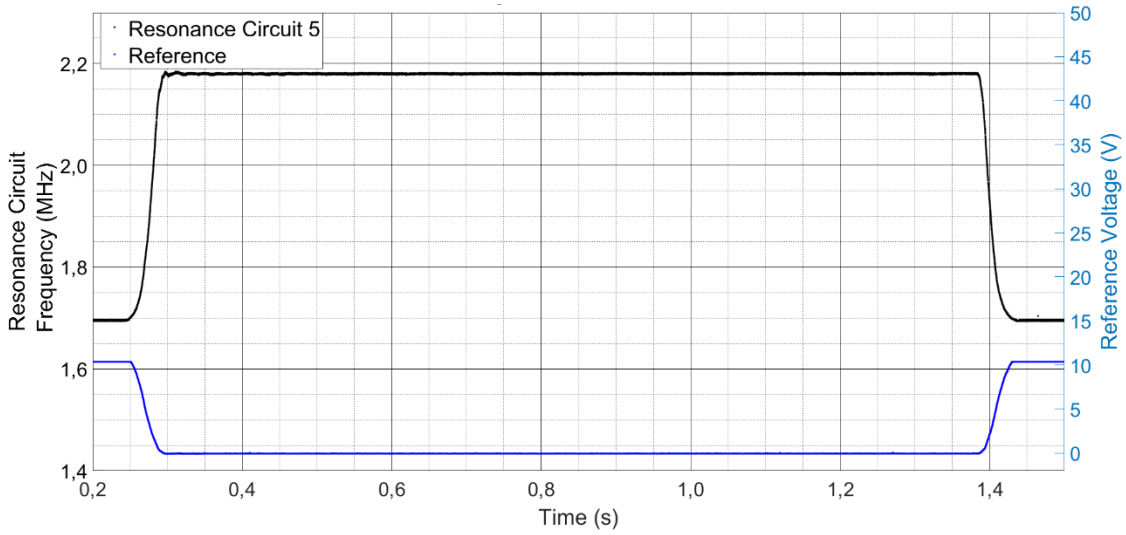

Figure 47: A/D converter output as a function of time while lowering and lifting the

SPCB.

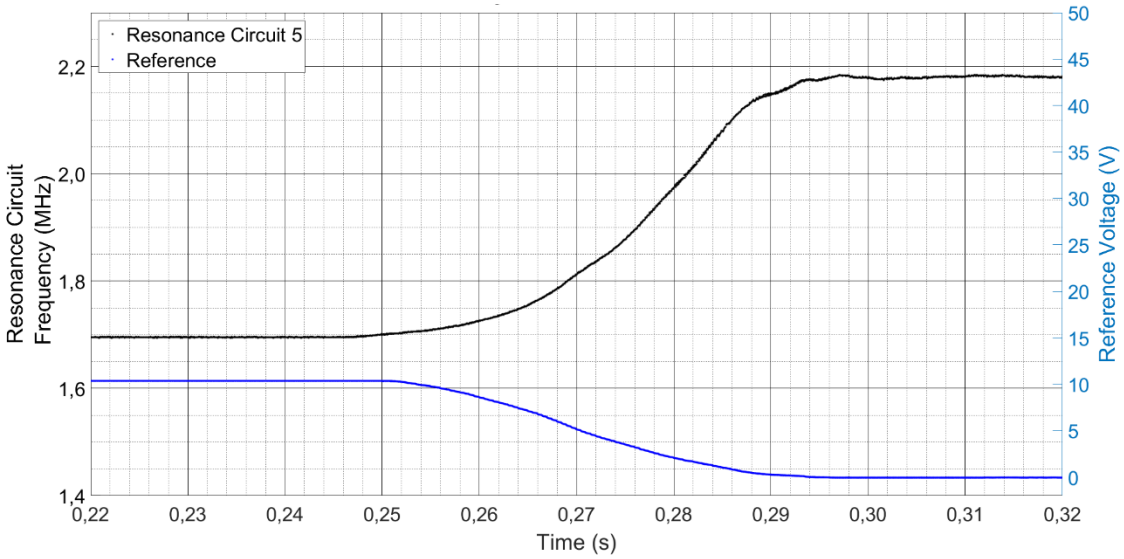

Figure 48: A/D converter output as a function of time while lowering the SPCB. This is Figure 47 zoomed in on the start of lowering.

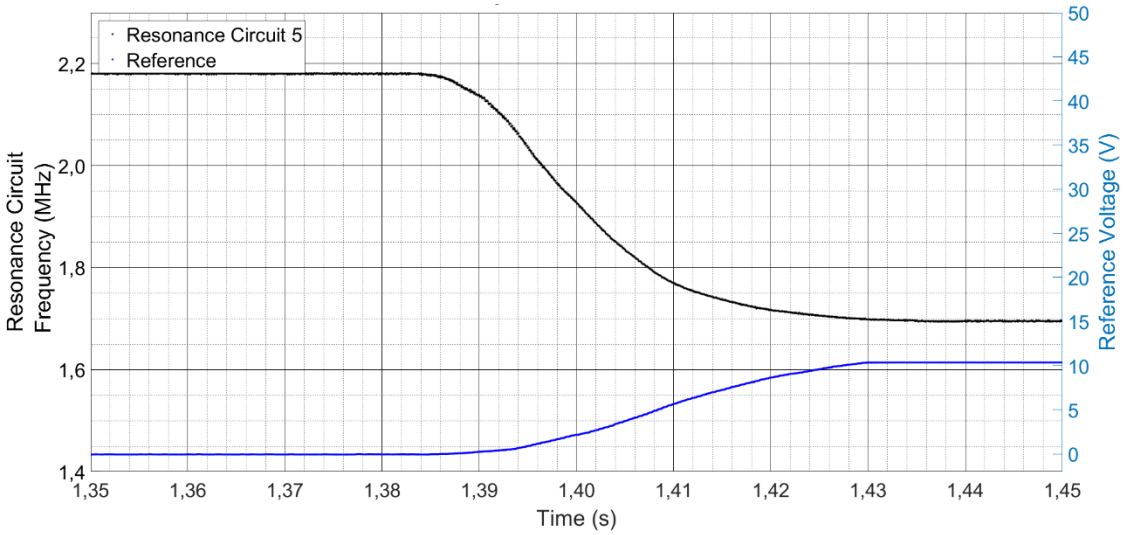

Figure 49: A/D converter output as a function of time while lifting the SPCB. This is Figure 47 zoomed in on the start of lifting.

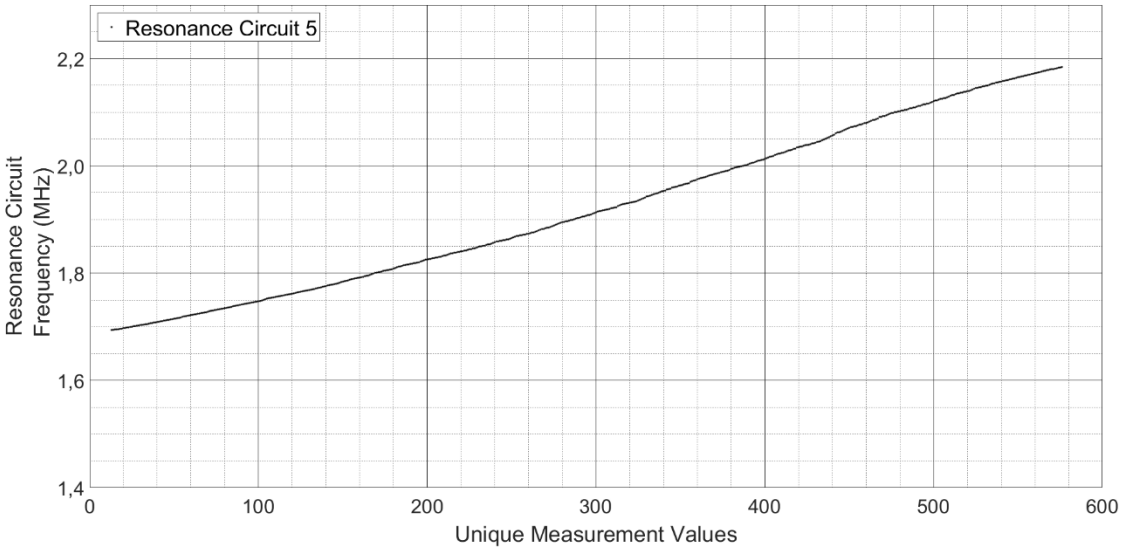

Figure 50: unique A/D converter output values of Figure 47.

C Response Time Results

The A/D converter output value at t_3 can be calculated with

$$y_3 = \frac{(t_2 - t_1 - t_{switching})y_1 + (t_3 - t_2 - t_{PCP})y_4}{t_3 - t_{PCP} - t_1 - t_{switching}} \quad (19)$$

where $t_{switching} = 28{,}4$ ns is the time which the solid-state switch requires to start conducting after receiving a control signal, y_1 is an A/D converter output value before change in the system y_3 is an A/D converter output value after a response time and y_4 is an A/D converter output value when the output has stabilized.

Following values are calculated from rotor position sensing tests:

Response time t_{R1}:

$$t_{R1} = t_3 - t_2 \quad (20)$$

response time t_{R2}:

$$t_{R2} = t_4 - t_2 \quad (21)$$

Test 10

Table 30: specifications of SPCB in test 10.

Shape of sensing coils	Hexagonal
Number of sensing coils	1
Air gap [mm]	1,47
Conversion time t_c [µs]	100
Number of sensing coil turns	11
Inductance L [µH]	11,68
Quality factor	26,25
Capacitance [pF]	1000

Table 31: measurements of test 10.

$\bar{t}_M$ [µs]	99,2430
t_1 [ms]	14,80
t_2 [ms]	14,87
t_3 [ms]	14,91
t_4 [ms]	15,01
Response time t_{R1} [µs]	40
Response time t_{R2} [µs]	140

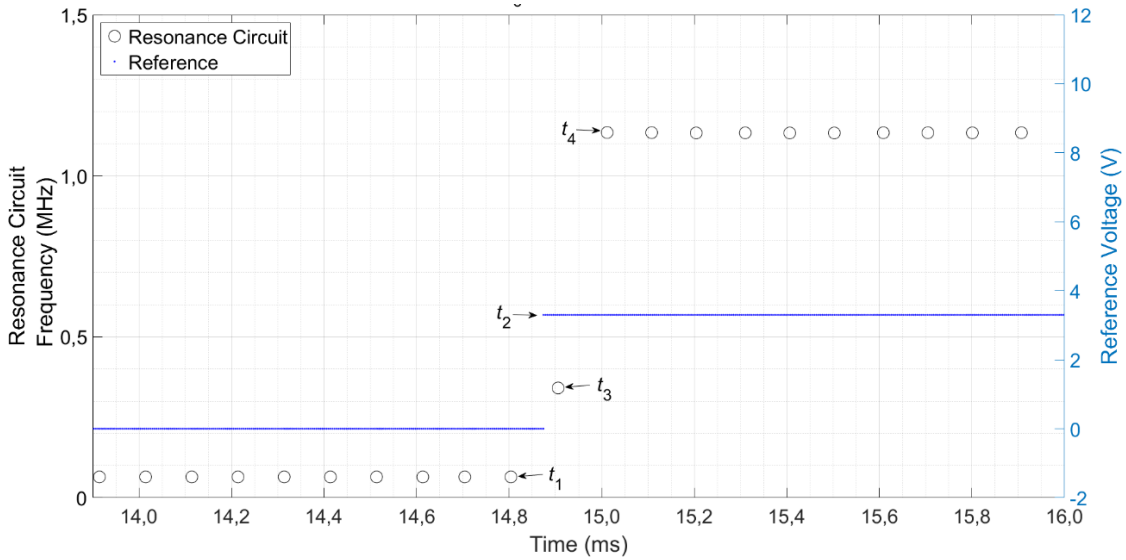

Figure 51: response time test above a flat aluminum surface.

Test 11

Table 32: specifications of SPCB in test 11.

Shape of sensing coils	Hexagonal
Number of sensing coils	1
Air gap [mm]	0,00
Conversion time t_c [µs]	200
Number of sensing coil turns	11
Inductance L [µH]	11,68
Quality factor	26,25
Capacitance [pF]	1000

Table 33: measurements of test 11.

$\bar{t}_M$ [µs]	199,3368
t_1 [ms]	25,89
t_2 [ms]	26,00
t_3 [ms]	26,08
t_4 [ms]	26,29
Response time t_{R1} [µs]	80
Response time t_{R2} [µs]	290

Test 12

Table 34: specifications of SPCB in test 12.

Shape of sensing coils	Hexagonal
Number of sensing coils	1
Air gap [mm]	1,47
Conversion time t_c [µs]	200
Number of sensing coil turns	11
Inductance L [µH]	11,68
Quality factor	26,25
Capacitance [pF]	1000

Table 35: measurements of test 12.

$\bar{t}_M$ [µs]	199,3530
t_1 [ms]	133,0
t_2 [ms]	133,1
t_3 [ms]	133,2
t_4 [ms]	133,4
Response time t_{R1} [µs]	100
Response time t_{R2} [µs]	300

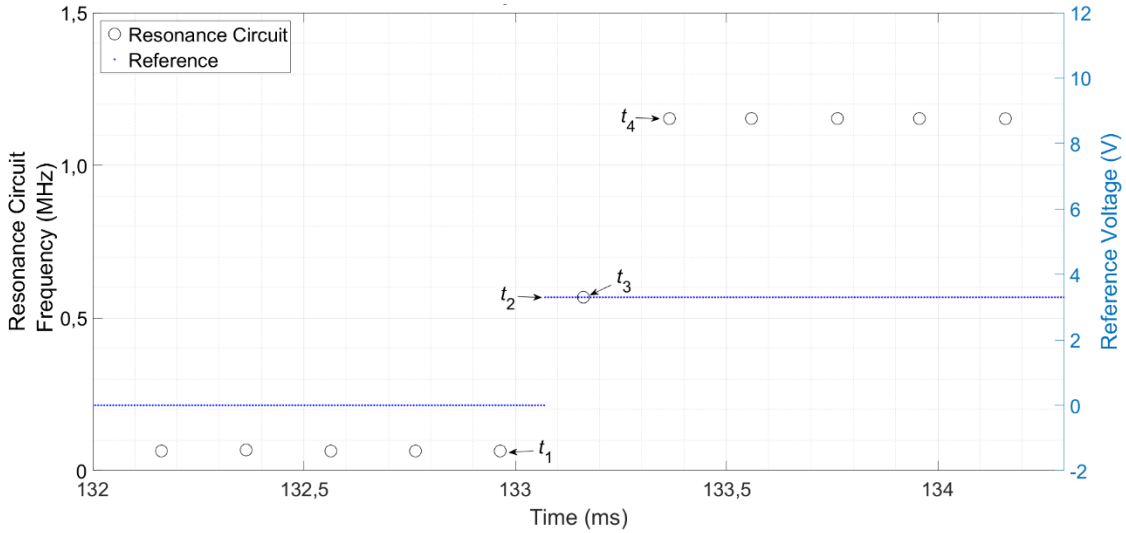

Figure 52 response time test above a flat aluminum surface.

Test 13

Table 36: specifications of SPCB in test 13.

Shape of sensing coils	Hexagonal
Number of sensing coils	1
Air gap [mm]	4,80
Conversion time t_c [µs]	200
Number of sensing coil turns	11
Inductance L [µH]	11,68
Quality factor	26,25
Capacitance [pF]	1000

Table 37: measurements of test 13.

$\bar{t}_M$ [µs]	199,3454
t_1 [ms]	82,56
t_2 [ms]	82,67
t_3 [ms]	82,76
t_4 [ms]	82,96
Response time t_{R1} [µs]	90
Response time t_{R2} [µs]	290

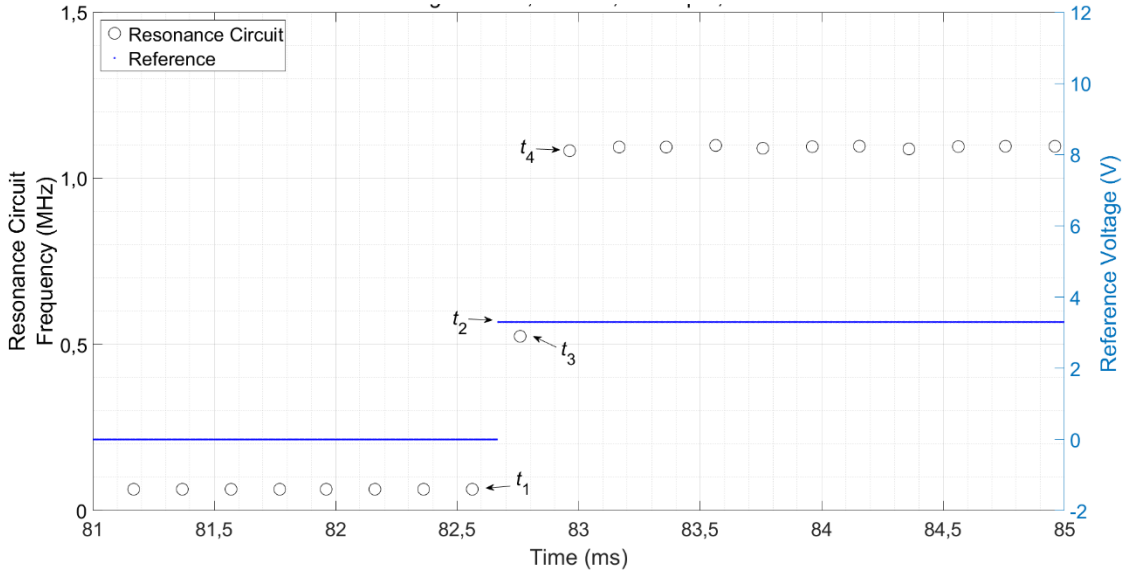

Figure 53 response time test above a flat aluminum surface.

Test 14

Table 38: specifications of SPCB in test 14.

Shape of sensing coils	Hexagonal
Number of sensing coils	1
Air gap [mm]	7,80
Conversion time t_c [µs]	200
Number of sensing coil turns	11
Inductance L [µH]	11,68
Quality factor	26,25
Capacitance [pF]	1000

Table 39: measurements of test 14.

$\bar{t}_M$ [µs]	199,3843
t_1 [ms]	70,23
t_2 [ms]	70,33
t_3 [ms]	70,43
t_4 [ms]	70,64
Response time t_{R1} [µs]	100
Response time t_{R2} [µs]	310

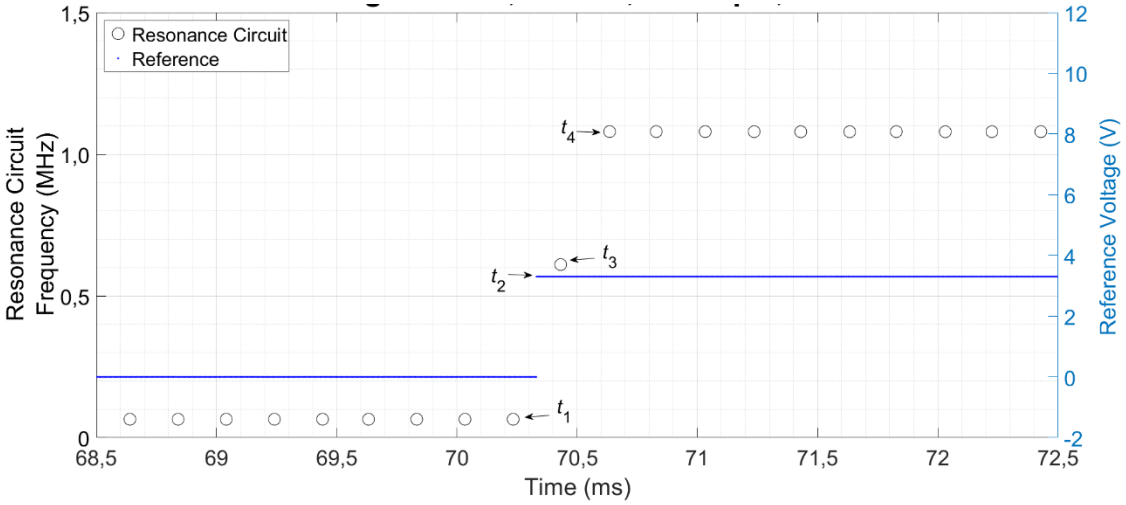

Figure 54 response time test above a flat aluminum surface.